Journal of Materials Chemistry C

ROYAL SOCIETY OF CHEMISTRY

REVIEW

View Article Online
View Journal | View Issue

Cite this: J. Mater. Chem. C, 2023, 11, 8724

White lasing – materials, design and applications

Alina Szukalska and Jaroslaw Mysliwiec *

Received 10th March 2023,
Accepted 24th May 2023

DOI: 10.1039/d3tc00872j

rsc.li/materials-c

In the last few years, the sources of directional, coherent, and powerful White Light Emission (WLE) have been extensively studied due to their many possible applications in optoelectronics, imaging, and lighting. Future directions for research include the development of the WLE sources for the novel concept of fully wireless technology of data transmission entitled Light Fidelity (Li-Fi). The combination of different color-emitting laser dyes, together with compatible materials with targeted optical properties, can lead to the construction of different white lasers (WL), which is still a very novel topic. In the last few years, since the discovery of the first WL (2015), a rapid evolution of scientific interest from the topic of white fluorescence to white lasing has been noticed. This work aims to present these advancing devices, obtained using organic, inorganic, and hybrid systems. The scientific discussion includes an emphasis on different laser constructions, the specification of different used materials, and the analysis of their future applications.

1. Introduction

Nowadays, tunable, multicolor and especially white light sources play a crucial role in scientific, technological, and industrial areas. Modern technologies continuously search for new materials to provide breathtaking colors on displays, smart devices, projectors, and many more. Color tuning gives the ability to adjust lighting to individual preferences and it is useful in everyday life as well as high-tech technologies. The specific applications and systems relying on interactive and easy light control are in high demand and white laser realization has become the ultimate goal for many scientific groups.

Soft Matter Optics Group, Institute of Advanced Materials, Wroclaw University of Science and Technology, Wyb. Wyspianskiego 27, 50-370 Wroclaw, Poland. E-mail: jaroslaw.mysliwiec@pwr.edu.pl

Alina Szukalska

Alina Szukalska started her scientific career in 2015 in Advanced Materials and Engineering Group at Wroclaw University of Science and Technology. She obtained a doctorate entitled "Light amplification in dye-doped liquid-crystalline systems" in the discipline of Chemical Science in 2019. Currently, Alina Szukalska continues her didactic and scientific work at the University of Science and Technology. Her scientific interest covers liquid crystals, laser dyes, and polymers, creating systems for light amplification. Her main motivation is to obtain organic systems for white lasers and white fluorescence.

Jaroslaw Mysliwiec

Prof. Jaroslaw Mysliwiec. PhD in Chemistry, Full Professor in Materials Science, employed at the Wroclaw University of Science and Technology, head of the Soft Matter Group (SMOG). His research activity is focused on linear and non-linear optical effects in novel push–pull types of molecules, photochromic polymers and biopolymers, liquid crystalline systems, and on the investigation of the light amplification properties (amplified spontaneous emission, lasing and random lasing) of organic systems. Co-author of about 130 scientific papers and 3 patents. Currently coordinator of a national scientific project founded by the National Science Center – Poland, related to the light amplification and white lasing in liquid crystalline materials. He has been awarded by the Polish Ministry of Science, and Foundation for Polish Science. Member and chair of scientific committees of several international conferences.

Adjustment of white and colorful emission from both organic and inorganic materials is often required for use in displays,[1–3] superbright solid-state lighting,[4] imaging[5], anti-counterfeiting,[6,7] fluorescence labeling for bio-imaging,[8] chemosensors,[9] environmentally friendly[10] and biomedical applications.[11,12] In the topic of displays, newer materials and their combinations are pursued to provide bright and saturated colors, high energy efficiency, and excellent contrast. It is worth distinguishing the approach presented in Angewandte Chemie.[13] The article describes a new method for producing organic printed core–shell heterostructure arrays that can serve as building blocks for full-color laser display panels. The method involves selectively printing organic ink solution droplets on hydrophobic substrates, resulting in micro-laser arrays with well-defined spherical cap morphology and smooth surfaces. By incorporating different luminescent dyes into the ink, the micro-size arrays can provide lasing in a wide range of colors. They can be mixed to produce vivid displays with excellent color saturation offering all-color laser display panels. Quantum Dots (QDs) have great potential applications because of their unique electrical and optical properties, which are now commercially investigated for novel display and lighting areas[14,15] as well as for solar cells,[16,17] white light-emitting-diodes, lasing,[18] bio-imaging and diagnostics. Many of the applications discussed here function perfectly using the principle of Light Emitting Diodes (LED) and famous Organic Light Emitting Diodes (OLED) illumination.[19–22] The most effective and practical source of excellent color fidelity for lighting and display applications is solid-state lighting (SSL) technology based on LEDs. Unfortunately, the "efficiency droop" severely restricts the performance of the LEDs.[23,24] It is a phenomenon where the efficiency decreases rapidly, as the current increases. It is well known that low currents (of just tens of milliamps) are the most effective for running LEDs. Therefore, it limits their operation to relatively lower input power densities. The driving currents used by the LED lighting sector are significantly higher than those for which efficiency is ideal due to practical considerations. Although experts are unable to identify the reason for the efficiency loss, LED producers are eager to overcome this very challenging compromise.

Future technologies place great hopes in laser light which can become an alternative source, since it exhibits non-questionable advantages like a wider achievable color gamut, a higher contrast ratio, and more vivid colors[25] in comparison with LEDs. Also, the need for high efficiency at high current densities ($\sim$kA cm^{-2}) makes lasers the most efficient converters of electrical to optical energy. Indoor lighting is associated with diffused and not powerful light, while it has been already proven that laser light is comfortable with the human eye as the commonly used LED lights.[25] Moreover, the white laser allows for obtaining 70% more colors than modern industry standards for displays and monitors. This highlights the possibility of taking advantage of the undisputed properties of laser light, which are *e.g.* directionality, coherence, and high power in future communication, lighting, and display technologies. The phenomenon of extremely nonlinear optical processes is the foundation of the current technology used to generate white-light lasers. To get a broadening of the emission spectrum and span the range of visible light, they need a very high input power of light.[26] For instance, by focusing high-power femtosecond pulses on transparent materials, white-light pulses can be produced. By using this method, white-light lasing sources have been made commercially available for use in research. Nonlinear optical processes do have disadvantages such as their large bulk and expensive production and operation.[27,28] Hence, many new materials which possess the properties of being easy, low energy consuming, affordable and tunable are being sought. Another use of lasers is their utilization as a light source in a room and a communication channel at the same time. This is why the Li-Fi concept of delivering the information as in a standard Wi-Fi network is currently extensively studied. In comparison, Li-Fi has about 10 times faster operating time.[29–31] By following this idea, thanks to the great energy and optical efficiency of lasers, it can be even pushed further, making it 10 to 100 times faster. Li-Fi becomes one of the main technological improvements on the market in the upcoming years. However, to be able to continue developing the field based on multicolor and white light emission, there is a constant need for a good understanding of materials, their compatibility, the possibility of combining into well-thought-out systems, determining their spectroscopic properties, and the role of optical pumping.

In this review, the main goal is to present the different ideas and approaches to creating fully functional white light emitting devices on the way of Stimulated Emission (STE), Amplified Spontaneous Emission (ASE), or lasing. Overall, a good understanding of possibilities to obtain the white lasing and the technological needs is crucial for the progress and development of new ideas. For this purpose, it is worth looking at the basics of material engineering, *i.e.* compatibility, selection of materials, their properties, discussion of matrices for lasing, emission stability, and tunability. Undoubtedly, an important aspect is also multicolor emission, which has applications in many fields of optoelectronics.

2. Resonators and mechanisms

2.1. Different WL-resonators

The classic, typical design of the laser cavity refers to the Fabry–Perot resonator. It is formed of flat, parallel mirrors that are both highly reflective and semi-permeable (one of them has a reflectance value close to 100%). The light is reflected multiple times from the mirror surfaces. Then, the reflection interference occurs and the waves that resonate with the cavity are amplified. The active material in the laser serves as the amplifier, ensuring population inversion. Positive feedback in the laser can be achieved unconventionally by using a scattering, disordered medium to replace the standard laser cavity. The phenomenon is well known in the literature as Random Lasing (RL). The kind of RL cavity has a specific gain medium, which might be a laser dye, dedicated for multiple scattering to occur. The pump light is diffusively scattered in the system and creates the gain region (see Fig. 1). When a photon travels inside the gain region, it is amplified, while it travels outside the gain region, it is non-constructively scattered. There is a

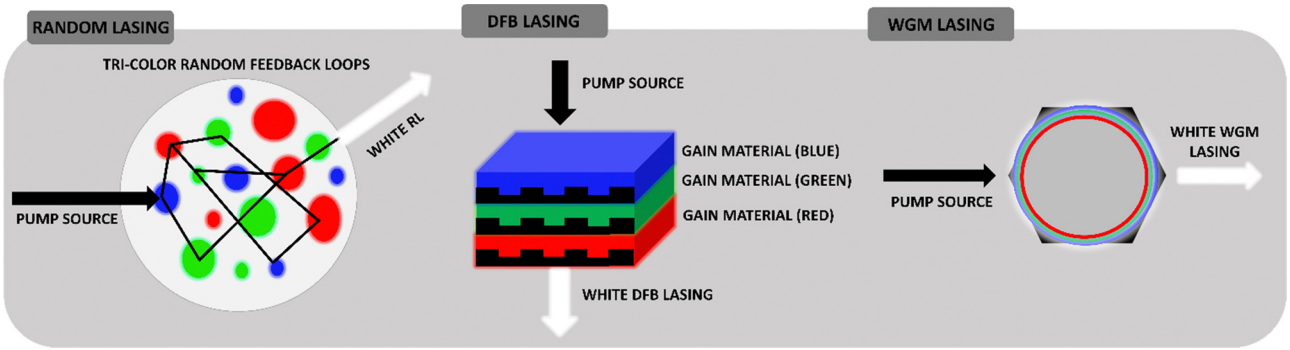

Fig. 1 Different resonators *via* white lasing – Random Lasing, DFB and WGM.

high probability that the photons will enter again the gain region to be re-amplified. There are two types of RL occurrences: non-resonant/incoherent and resonant/coherent.

Coherent RL manifests as multiple peaks with distinctively narrowed structures. The gain medium causes photons to return to their original starting place, a phenomenon reminiscent of the Fabry–Perot cavity. The incoherent RL spectrum, however, is displayed as a narrow peak that is centered in the highest frequency range. The main advantages of RLs are the scattering-dependent spectral characteristics, the easy process of fabrication, and the relatively cheap components. It is justified that in real conditions it is difficult to get rid of all defects, spontaneously formed structures and all other elements that introduce disorder in the system. Random lasers are therefore ideal, allowing the use of seemingly unnecessary elements to create a resonator. Practically, the laser is associated with monochromatic emission, while the white light itself is the opposite of monochromaticity since it is composed of three primary colors (Red, Green, Blue – RGB). Today's expectations concern strong, coherent light sources, easily tunable in terms of intensity and color (more about this in the Applications section). Therefore, the implementation of the White Random Lasing (WRL) should be based on finding three gain materials (instead of the classic, one gain provider) and integrating them into a useful and precisely planned matrix. As shown in the literature, an important aspect is trying to separate the gain components to counteract energy transfer. Thus, three-color media can be used as randomly distributed scatterers, for example, nanoparticles, aggregates, crystals, liquid crystalline domains, and droplets. Such examples of WRL realization will be discussed further.

Distributed feedback (DFB) resonator is another example of an optical resonant cavity. Compared to the Fabry–Perot architecture, DFB lasers consist of an active layer made of a diffraction grating structure. The periodic changes in refractive index, which reflect the precise wavelength, are its defining feature. As a result, DFB produces the precise, single-needed wavelength. It is widely believed that this sort of laser cavity is more stable than Fabry–Perot in applications requiring one-mode lasing, such as waveguiding. The compact format of WL involves the coordination of three, individual RGB and DFB lasers which are varied by the thickness of gain layers. As it is presented in the scheme, the lasers form a stack. Each DFB laser emits concurrently while being optically pumped, and because their output overlaps, a combined white emission can be seen.

Based on the phenomenon of total internal reflection, Whispering Gallery Mode (WGM) resonators are a type of optical cavity in which light can be steered around and circulated. Such a phenomenon occurs at the curved cavity surfaces. As a result, WGM can be found in the sphere, ring, or even hexagonal[32] gain materials, which have a higher refractive index than the surrounding environment. This example's Q factor can go as high as 10^{10}, which is seen to be a major benefit. White WGM lasers can be realized by partitioning three kinds of light-emitting nanoparticles[32] or polymers[33] in nested, compact microcavities. This results in the high Q factor, controlled, tunable, low threshold, narrow resonant spectral line laser systems.

2.2. Energy transfer and its role in WRL

The non-radiative energy transfer occurring from long-distance interactions between the excited donor (D) and acceptor (A) molecules (dipole–dipole relation) in the ground state is the basis of the Förster Resonance Energy Transfer (FRET) phenomenon.

Scheme based on[34] represents (see Fig. 2a) the general FRET mechanism.

For the D–A pair, the following criteria must be fulfilled to effectively transfer energy on the way of FRET:

•The donor emission spectrum must at least partially coincide with the absorption spectrum of the acceptor. The degree to which the spectra overlap is referred to as the spectral integral of the overlap (Fig. 2b). A higher degree of J increases the probability of FRET.

$$J = \int J(\lambda)\mathrm{d}\lambda = \int \mathrm{FD}(\lambda)\lambda^4 \in A(\lambda)\mathrm{d}\lambda$$

where FD is the normalized photoluminescence emission of the donor, $\in A$ is the spectral extinction coefficient of the acceptor, and λ is the wavelength.

•The FRET efficiency (E) is calculated by the equation $E = 1/1 + (R/R_0)^6$, where R_0 is the Förster radius and R is the actual distance between the donor and acceptor molecules. FRET reaches its highest efficiency when R is less than R^0, which is the donor–acceptor distance equivalent to 50% efficiency and falls with R^{-6}. As a result, FRET occurs only at very small distances, up to 10 nm (see Fig. 2c).

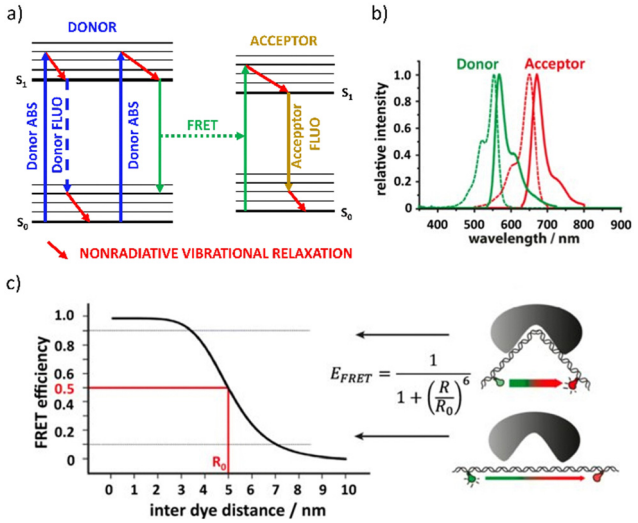

Fig. 2 (a) Scheme demonstrating the FRET mechanism. Reproduced (or Adapted) with permission[34] 2019, Springer Nature.; (b) spectral overlap between the emission spectrum of a donor dye (green continuous line, Alexa Fluor 555) and absorption spectrum of an acceptor dye (red dashed line, Alexa Fluor 647) that leads to FRET. Reproduced (or Adapted) with permission,[34] 2019, Springer Nature; (c) FRET efficiency as a function of donor–acceptor distance (taking a Förster radius R_0 as 5 nm). Reproduced (or Adapted) with permission,[34] 2019, Springer Nature.

•To determine the distance between a FRET pair, E can be calculated by several different methods. Two of them are shown here:

$$E = 1 - I_{DA}/I_D = 1 - \tau_{DA}/\tau_D$$

where I_{DA} and I_D are the molar concentration normalized emission intensities of the donor with and without the acceptor, respectively. Moreover, the FRET process also changes the fluorescence lifetime of the donor due to the presence of a competing pathway for the donor to relax back to the ground state. Therefore, fluorescence lifetime measurements can be used to calculate the FRET efficiency using the above equation, where τ_{DA} and τ_D are the donor's fluorescence lifetime with and without the acceptor, respectively.

•The chromophore centers of the molecules must be located in appropriate mutual spatial orientation.

Most often, the spectra of the materials show overlapping in terms of both the absorption and the absorption-fluorescence spectra. This creates desired conditions for FRET occurrence and can be effectively measured and confirmed by examining the fluorescence lifetime of specific samples. Multicolor and especially WL/WRL relies on the investigation of even three fluorescent compounds which create complex systems that require thorough analysis. As was demonstrated in the literature,[35] the substantial presence of FRET can be beneficial in quenching the laser emission of one or even two dyes and, as a result, in spectrum averaging. This results in a visible single laser emission maximum with a significantly increased half-width. The goal of the white laser is to produce three distinctly separated narrow spectra with maximal emission in the blue, green, and red ranges. This approach guarantees good control over emission tuneability. As a result, in the case of white light emission, FRET may be undesired.

The energy transfer can be dynamically tuned by changing the qualitative and quantitative composition of the gain materials or by the pumping condition. In the case of obtaining laser emission in white color, various strategies for separating emissive chromophores can be used, such as separation of tricolor free-standing films,[36] simple use of the spacers[33] or stacking of the layers,[37,38] investigation of different nanoparticles embedded in the matrix,[39–41] building the separated compact systems, such as microfluidic channels[42] or taking advantage from the natural phase-separation process, relying on hydrophobic/hydrophilic properties of selected materials.[38]

2.3. Up-conversion of energy for RGB and WL

A process where light can be emitted with photon energies higher than those of the light generating the excitation is called up-conversion. Upconverting materials are widely used in many applications, from electronics, optoelectronics, and solar cells to medicine.[43–50] However, these applications require different properties such as varied emitting colors, lifetimes, or the quantum yield of luminescence. Therefore, the key is the intentional design, modification, and creation of materials to obtain desired characteristics. It can be realized through deliberate co-housing phosphors with optically active or passive ions. In optical imaging of biological preparations, materials for the up-conversion process are used as markers to convert phosphors. These inorganic nanocrystals have a transparent host crystal lattice that has been doped with trivalent or transition metal lanthanide ions. The up-conversion processes in nanostructures need to be researched and comprehended to produce phosphor up-converters with precisely defined photophysical parameters (wavelength and emission intensity).[51]

Typically, trivalent, alkaline rare earth ions (REI) or selected transition materials are used as dopants for the host material. Halides (*e.g.* $NaYF_4$, YF_3, LaF_3) function as leading hosts due to their low lattice phonon energy which decreases energy losses by reducing the possibility of non-radiative multi-photon relaxation. For RGB/White Lasing applications, it is worth discussing the selection of the dopant ion, as this parameter determines the color of the emitted light. The photoluminescence properties of the lanthanides are determined by the 4f electrons.[52,53] The appropriate structure of the energy levels of Er^{3+}, Tb^{3+}, Tm^{3+}, and Ho^{3+}, as well as Pr^{3+}, Nd^{3+}, and Dy^{3+}, makes these ions suitable for upconverting materials. To further increase the efficiency of the up-conversion, the phosphors are doped with sensitizers, Yb^{3+} ions, which absorb ten times more radiation at a wavelength of 980 nm than Er^{3+} ions.[54] Moreover, in the crystals doped with Yb^{3+} ions, there is no observed strong luminescence quenching effect associated with an increase in the dopant concentration (which can be noticeable for other REIs). Therefore, a high level of activator excitation can be obtained by doping with a sensitizer.[51,54] The energy level of $^2F_{5/2}$ Yb^{3+} is occupied by the absorption of radiation at a wavelength of 980 nm. For example, the energy levels of Yb^{3+} $^2F_{5/2}$ and Er^{3+} $^4I_{11/2}$ are nearly in the perfect resonance, resulting in efficient energy transfer to Er^{3+} ions. This pair is therefore very effective in the context of efficient anti-Stokes photoluminescence. To obtain high

up-conversion efficiency, the number of sensitizing ions and activators in the host crystal lattice must be optimal.

The emission intensity increases with the increasing concentration of activator ions (*e.g.* Er^{3+} or Tm^{3+}), but their too-high concentration leads to the quenching caused by the cross-relaxation (CR) process between adjacent ions. The ratio of the intensity of the emission of the different colors can be fine-tuned by changing the distance between the activator ions (*i.e.* the level of doping). The Yb^{3+} sensitizer is not sensitive to concentration quenching, as mentioned earlier; therefore, its concentration may be many times higher than that of the activator ion. Ideally, the activator ions should be surrounded by the maximum amount of Yb^{3+} ions to increase the efficiency of the ETU (Energy Transfer Up-conversion) process.[55–61] The described materials and processes have been demonstrated in.[32,62] Importantly, each dopant ion has several emission states and each of the relaxation paths gives a different emission color. This allows for appropriate system design and effective color tuning, which is an undoubted advantage in the context of obtaining white light. An example of a very interesting design of a white light laser system is referred to in ref. 32 where microrods with six flat surfaces and hexagonal pyramid structure ends were used. Fig. 3a shows the mapping results and the photograph of Yb, Eu, Er, and Tm elements, which are uniformly distributed inside the microrods. The sensitizer, Yb^{3+}, is chosen because it absorbs light at a wavelength of 980 nm. Eu^{3+}, Er^{3+}, and Tm^{3+}, respectively, are the sources of RGB emissions.

The energy of the photons of the host crystal lattice can also influence the dominant path of relaxation. For example, green Er^{3+} emission (at 520 and 540 nm) is dominant in fluoride – low phonon energy materials because the multi-phonon relaxation processes required to fill the red luminescence emitting level ($^4F_{9/2}$) are rather unlikely due to relatively large energy gaps ($^4S_{3/2} \rightarrow {}^4F_{9/2} \sim 3200\ cm^{-1}$, $^4I_{11/2} \rightarrow {}^4I_{13/2} \sim 3600\ cm^{-1}$). Red emission may dominate in host materials with higher phonon energy. Also, the external factors (*e.g.* surface defects and pollution) can lead to a reduction in the ratio of the green intensity to the red emission line. In addition, the color intensity ratio of the emission is influenced by the energy density of the excitation source.

In Fig. 3b, the energy level diagrams of Yb^{3+}–Er^{3+}–Tm^{3+} tridoped β-$NaYF_4$ microrods (shown schematically in 3a) are demonstrated. Transitions from $^4F_{9/2}$ to $^4I_{15/2}$ (654 nm, red), $^2H_{11/2}$ to $^4I_{15/2}$ (520 nm, green), and $^4S_{3/2}$ to $^4I_{15/2}$ (540 nm, green) are all triggered by the presence of Er^{3+}. These two-photon absorption processes cause the red and green transitions. High Yb^{3+} concentrations are anticipated to favor the red emission peak, whereas low Yb^{3+} concentrations are anticipated to boost the green emission peak due to the influence of the cross-relaxation process. Tm^{3+} causes the transitions $^1D_2 \rightarrow {}^3F_4$ (450 nm, blue) and $^1G_4 \rightarrow {}^3H_6$ (475 nm, blue) to occur. The blue transition, on the other hand, undergoes a three-photon absorption process, which reduces its upconversion efficiency in comparison to the red and green peaks. The doping concentration of both Yb^{3+} and Tm^{3+} is chosen to enhance blue emission intensity to generate high-power white-light emission at a high excitation power. Then, to concurrently maximize RGB emissions with the same degree of intensity, the doping concentration of Er^{3+} is chosen.

Another interesting work of a random laser obtained in the $NaYF_4$:Yb/Er/Tm@$NaYF_4$:Eu core–shell nanoparticles assisted by Au/MoO_3 multilayer hyperbolic meta-materials is presented in Fig. 3c. The picture demonstrates the morphology of these materials with the use of a TEM (Transmission Electron Microscope). The highly monodispersed $NaYF_4$:Yb/Er/Tm@$NaYF_4$:Eu core–shell nanocrystals with a size of 20 ± 0.5 nm have been confirmed. In the composite nanoparticles, $NaYF_4$ functions as the host. A sensitizer that absorbs light at a wavelength of 980 nm is chosen, Yb^{3+}. Emissions from Tm^{3+}, Eu^{3+}, and Er^{3+}, respectively, give out green, red, and blue light. The relative ratios of the intensity of the resulting emission may be controlled by altering the emission ion concentration. The emission lines can be ascribed to the transitions shown in the earlier reports (Fig. 3d) as follows: blue ($^1G_4 \rightarrow {}^3H_6$ and $^1D_2 \rightarrow {}^3F_4$ of Tm^{3+}), green ($^4S_{3/2} \rightarrow {}^4I_{15/2}$ and $^2H_{11/2} \rightarrow {}^4I_{15/2}$ of Er^{3+}), and red ($^5D_1 \rightarrow {}^7F_5$ and $^5D_2 \rightarrow {}^7F_6$ of Eu^{3+}. Therefore, it is expected that the upconversion core–shell nanoparticles developed here would be able to produce a variety of light-emitting colors, including white light, by simply adjusting the ion concentration that emits light.[63]

2.4. Materials for white amplified spontaneous emission and lasing

2.4.1. Quantum dots. Quantum dots are semiconductor particles with diameters ranging from 2 nm to 10 nm. Due to their small size, quantum effects play a significant role in their optical properties. QDs emit light through a simple mechanism: when exposed to an external stimulus (light, electricity, *etc.*), electrons absorb enough energy to move from the ground state to the higher, excited state. In semiconductors, higher electron levels are found in the conduction band, which is separated from the lower orbits (valence band) by an energy break. This results in the formation of a local conduction region in which electrons can travel through the material, effectively conducting electricity. When these electrons return to their atomic orbits, energy is released in the form of a photon whose energy (and thus color) depends on the amount of energy released – the difference between the energies of the individual electron orbits. The mentioned levels are quantized – the energy released by the electrons is constant for a given type of QDs. Therefore, the color depends on the material and the size of the QDs. Exemplarily, the QDs reaching a size of 5.6 nm emit lower energy photons, resulting in red and orange photons color of emission. Relatively smaller QDs (*e.g.* 2.3 nm) emit higher energy photons responsible for the blue and violet emitted light. This property is directly related to the fact that a QD is a three-dimensional quantum well, with the QD diameter linked to the energies of discrete energy levels. The entire light spectrum can be produced simultaneously and appears as white light by combining a variety of sizes of quantum dots in the same sample.[64]

Based on the literature, the hydrothermally produced carbon dots (CDs) with tunable photoluminescence (PL) and a quantum yield of up to 35% in water (Fig. 4a) are demonstrated. Under a single-wavelength UV light, these separated (with the silica

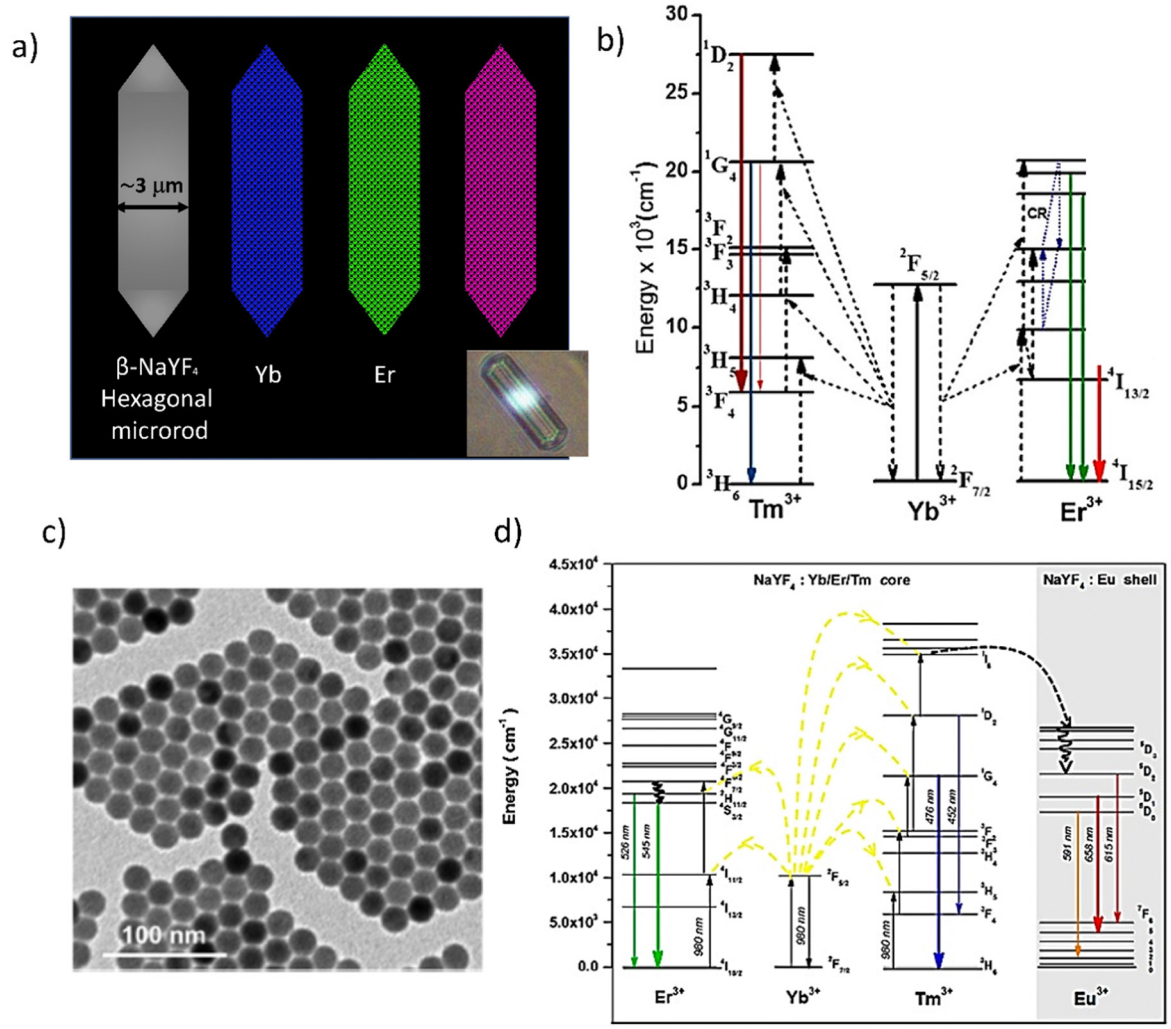

Fig. 3 (a) The schematic presentation of different monochromatic microrods containing the RGB components for up-conversion with the photograph as inset. Reproduced (or Adapted) with permission,[32] 2017, ACS; (b) energy level diagrams of Yb^{3+}–Er^{3+}–Tm^{3+} tridoped β-$NaYF_4$ microrods. Reproduced (or Adapted) with permission,[32] 2017, ACS; (c) a white light-emitting device – the TEM and the (d) energy diagrams and Schematic illustration of the photon upconversion mechanism in a $NaYF_4$:Yb/Er/Tm@NaYF4:Eu core–shell nanocrystal. Reproduced (or Adapted) with permission,[62] 2018, ACS.

column chromatography) CDs exhibited brilliant and stable luminescence in gradient colors ranging from blue to red. They had a high optical homogeneity, which means that each sample had only one peak in the PL excitation spectra, one peak in the excitation-independent PL emission spectrum, and similar monoexponential fluorescence lifetimes. Another example of multicolor-oriented synthesis leads to the perovskite QDs,[67] which is presented in Fig. 4b. Perovskites are great candidates for the WLE because they allow for heterogeneous compositions, where partial substitutions at any of the A, B, and X-sites can result in bandgaps (and thus emission peaks) centered at any point within this range of values. Indeed, these mixed-composition perovskites are used in many of the most promising and cutting-edge studies. The emission spectrum of cesium lead trihalide ($CsPbX_3$) perovskite QDs, for example, can be adjusted across the whole visible color gamut by altering the halide ratio.[67] Fig. 4c illustrates the optical properties of metal carbides quantum dots (MQDs) with and without passivating treatment, including absorption and photoluminescence. Furthermore, with the help of internal reabsorption and reemission, the photoluminescence was widened, particularly in the longer wavelength area, with the cutoff edge reaching around 700 nm. This means that the photoluminescence of MQDs extends into the red color spectrum. Fig. 4c shows pictures illuminated at different wavelengths, with the results that under excitation wavelengths less than 400 nm, the samples displayed near-white color that was hybridized by broadband photoluminescence. Combined with the greater photoluminescence under shorter wavelength excitation, it can intuitively be concluded that an excitation source at a wavelength shorter than 400 nm should be desirable for the construction of a white laser if broadband optical feedback was built.[16]

2.4.2. Liquid crystals. Currently, the knowledge of Liquid Crystals (LCs) is quite advanced. Back in the day, LCs became the basic materials for the operation of LCD TVs. These days, LED, Quantum Dot Light-emitting Diode (QLED), and OLED display technologies become serious competitors for LC-based monitors.

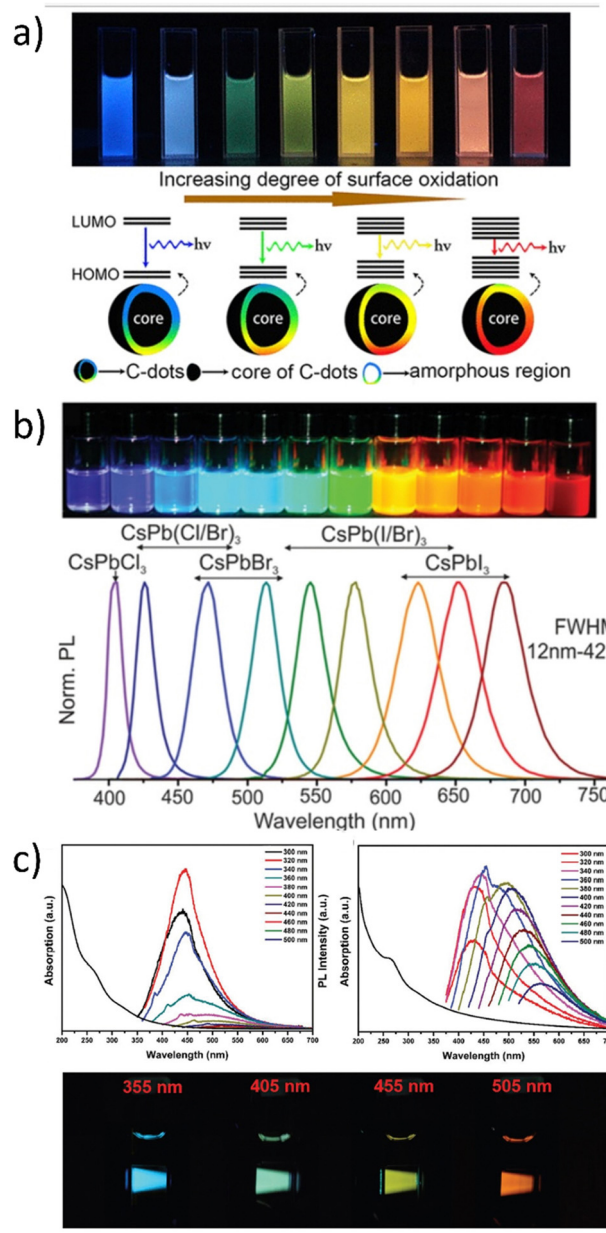

Fig. 4 (a) Full-color light-emitting carbon dots with a surface-state-controlled luminescence mechanism. Reproduced (or Adapted) with permission,[65] 2016, ACS; (b) Colloidal perovskite $CsPbX_3$ NCs (X = Cl, Br, I) exhibit size- and composition-tunable bandgap energies covering the entire visible spectral region with narrow and bright emission: colloidal solutions in toluene under a UV lamp (λ = 365 nm). Reproduced under terms of the CC-BY license.[66,67] 2020, Wiley. (c) UV-vis absorption (left side), PL spectra of V2C MQDs without passivating treatment in aqueous solutions and the pictures at different excitation wavelengths (xenon lamp). Reproduced or adapted with permission,[16] 2019, Wiley.

Following the initial studies of LCs, which still seem to be a fascinating matter, researchers confirmed their two fundamental properties. Namely, LCs show the ability to flow, while sustaining concomitantly the long-term orientational order, which is rather typical for solid-state crystals. Then, it was found that, according to these features, the spatial structure of liquid crystalline molecules is susceptible to the influence of various external fields. Some of the stimuli affecting the LC molecular alignment are *e.g.* temperature, lighting, mechanical stress, and the electric and magnetic fields. This property is priceable in the scope of the studies of multicolor/white-emitting LC systems presented here since it can significantly affect the obtained emission properties. In the guest–host systems, the LCs can play the role of the matrix for the precisely selected luminescent dopants. For the multicolor and white lasing, it is crucial to match three chemically and molecularly compatible dyes. Stephen M. Morris *et al.*[68] have demonstrated a technique for optical excitation with a single visible wavelength that results in simultaneous red, green, and blue laser emission from a liquid crystal band-edge laser (see Fig. 5a, b and c).

This study presents the results of WLE for three dyes, namely DCM, CM 540A, and CM 504 embedded in the LC matrix. The systems were characterized by their basic spectroscopic properties (Fig. 5a). In the LC hosts, the transition dipole moments of the dyes have shown positive order parameters resulting in preferred lasing along the photonic band edge at long wavelengths. The array pumping technique with a pitch gradient cell was utilized to create a single material system that produces RGB (or more colors) concurrently. When the sample is optically pumped at 430 nm, the LC laser array consisted not only of blue and red columns but also of the column of green (563 nm) and yellow spots (589 nm) (Fig. 5b). This effect is visible in Fig. 5c, presenting the multicolor laser emission coming from a cell.

Another example of a multicolor laser is demonstrated in.[35] Three laser dyes embedded in the LC host (see Fig. 5d) undergo a stimulated emission phenomenon when pumped by the single laser wavelength (450 nm). The examined system due to the near presence of all used luminescent dyes and varied relative weight-to-weight ratio shows great color tunability. Such work serves as the perfect example of liquid crystalline captivating properties investigation. The color of STE can be effectively tuned by the application of an electric field (Fig. 5e). As was pointed out, the unique attribute of LCs is that their initial molecular arrangement may be adjusted by applying a voltage to the LC cell. In a multicolor system, as shown in the example above, the emission color can also be controlled using the rotation of the molecules at very low voltage values (up to 10 V).

Fig. 5f presents very interesting multicolor tunability for the next generation of 3D displays. The authors suggest the utilization of Cholesteric Liquid Crystals (CLCs), which possess the ability to organize into either right-handed or left-handed helical superstructures, thereby enabling the creation of strong Circularly Polarized Light (CPL). The panels, crafted through the technique of micro template-assisted inkjet printing, comprise two sets of CLC microlaser pixel arrays that emit orthogonal Circularly Polarized (CP) laser emissions. By incorporating the corresponding gain dyes into CLCs with their left-/right-handed helical superstructures functioning as distributed feedback microcavities, Red-Green-Blue (RGB) CP laser emissions were attained. The two-color CP lasing emission (R + G) was produced by synchronously pumping the red- and green-emissive CLC microunits, as displayed in Fig. 5f. Similarly, other two-color

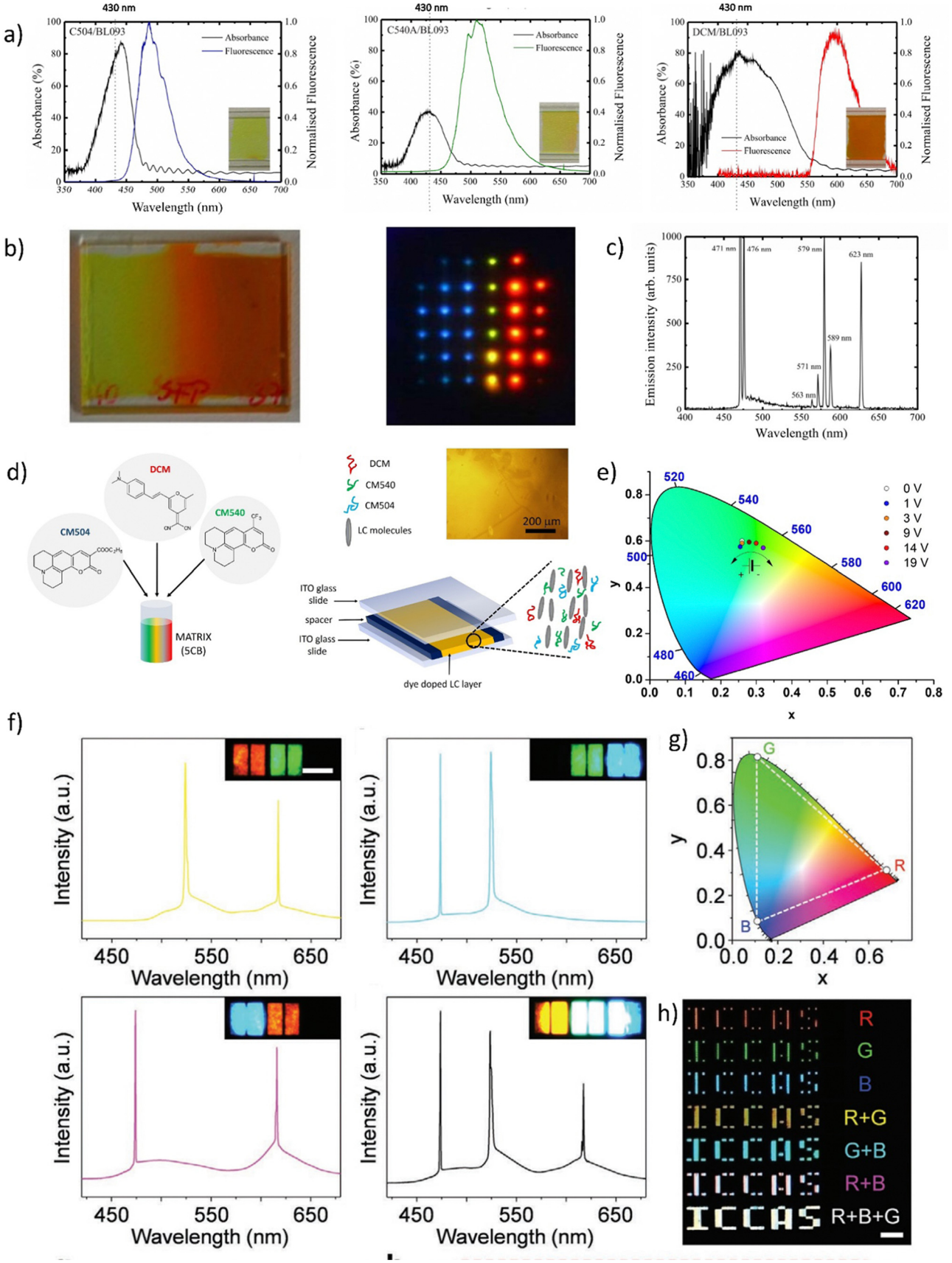

Fig. 5 (a) Absorbance and fluorescence of three dyes: CM504, CM540, and DCM doped to the nematic liquid crystal (BL093) host; (b) images of the gradient pitch liquid crystal laser cell, made by filling the cell with two different liquid crystals and dye mixtures from opposite sides together with an image of liquid crystal laser emission from the cell. (c) The emission spectrum, illustrating simultaneously occurring polychromatic laser emission when pumped at 430 nm using a lenslet array, lasing occurs in the cell. Reproduced (or Adapted) with permission,[68] 2008, OSA Publishing; (d) Presentation of the dye-doped LC system. Mixture contents: luminescent dyes CM504, CM540, and DCM embedded in liquid crystalline 5CB matrix; handmade LC cell construction. All molecules align planar according to the LCs domains. As an inset – an optical microscope image presenting homogeneity of LC's molecules in the cell; (e) tunable light emission controlled by applied DC voltage presented on CIE XYZ diagram (LC cells and three dyes in ratio 5 : 2 : 1; pumping fluence = 3 mJ cm^{-2}). Reproduced (or Adapted) with permission,[35] 2020, Elsevier; (f) full-color 3D laser displays based on Circularly Polarized lasing. The lasing spectra and corresponding PL microscopy images of different combinations of RGB CLC subpixels are presented. Red and green (top left), green and blue (top right), red and blue (bottom left), and red, green, and blue (bottom right) emissive CLC microunits. Scale bar: 100 μm. (g) Chromaticity of the lasing peaks extracted from RGB CLCs lasing spectra, shown as three white circles. (h) Far-field image of the "ICCAS" patterns of CLC pixel arrays composing different RGB CLC microunits. Scale bar: 1 mm. Reproduced or adapted with permission.[69]

CP lasing emissions (G + B, R + B) were obtained by selectively pumping the respective microunits in an individual RGB CLC pixel. Moreover, the integrated pumping of all microunits in an individual pixel led to the generation of three-color lasing (R + G + B). The chromaticity coordinates (Fig. 5g) of these RGB lasing spectra were computed and noted on the CIE1931 chromaticity diagram. Namely, for printed RGB CLC microlaser pixels the chromaticity coordinates are as follows: for Red (x = 0.686, x = 0.314), for Green (x = 0.110, y = 0.827) and for Blue (x = 0.113, y = 0.080). While for the widely used in industry chromaticity coordinates values are (x = 0.640; y = 0.330), (x = 0.300, y = 0.600), and (x = 0.150; y = 0.060) for R, G, B, accordingly.[70] The vast color gamut, defined by the chromaticity coordinates from the RGB lasing spectra, indicates that the fabricated CLC microlaser arrays are highly competent in producing vibrant 3D displays with exceptional color saturation. To evaluate the far-field color rendering of mixed emissions from multicolor microlaser pixels, actual-color images of CLC microlaser arrays were taken under laser irradiation (Fig. 5h).[69]

2.4.3. Luminescent dyes. In this review, a wealth of different luminescent (especially laser) dyes are referred according to the fact that they serve as great optical gain providers and compatible guests to the organic/inorganic or hybrid hosts. Their undoubted advantages are the huge variety, the constant updating base of their availability, and the possibility to continuously synthesize new chemical compounds. Fig. 6 presents multicolor tunability, obtained with the help of the different sets of luminescent dyes.

The color tuning presented in Fig. 6a is based on the three commercially available luminescent dyes: Stilbene 420 (SB420), Coumarin540 (CM540), and Rhodamine610 (R610). The system is realized *via* the injection of the three capillaries with the dye solutions. The multicolor mixing and WL can be achieved also by investigation of the different sets of dyes: DCJTB, R6G, and once again, SB420 with on-chip integration. The independent red, green, and blue lasing can be combined by selectively pumping two or three single segments, rendering the WRL effect. The photoluminescence spectra presented in Fig. 6c show the successfully completed attempt to obtain a trichromatic emission covering the whole part of visible light by using mixtures of various commercially available dyes (Coumarines (CMs): 440, 460, 153, R6G, Oxazine) combined with the Au–Ag Nanowires. The visible light spectrum range can be also covered by the use of three single, specially selected, commercially available dyes: CMs 480 and 500 and DCM (Fig. 6d). Fig. 6e there demonstrates the colorful set of samples, with three different dopants: SB420, CM540, and DCM. The dyes are separated by the classification of their hydrophilic/hydrophobic chemical nature to provide three spectral components, lasing simultaneously in the RGB range. The presented examples show a great interest in the literature concerning commonly known and referred dyes. As the idea of obtaining white light by optical pumping can be considered a relatively young and very promising topic, it is worth paying attention to how many interesting, also newly synthesized compounds can be used in the future to obtain WL.

2.4.4. Organic crystals. Organic crystals have emerged as a representative class of laser materials in recent years due to their unique properties. One of the key advantages of organic crystals is their ability to undergo self-assembly *via* non-covalent bonding interactions. Unlike covalent bonds, non-covalent interactions are typically weaker and more reversible. They allow for the formation of a variety of complex structures, highly organized at both the micro and nanoscale. This self-assembly process leads to the formation of micro and nanocrystals with well-defined sizes and shapes. Therefore, they become the ideal candidates for WLs since the morphological control of used materials seems a crucial parameter.

Currently, there are a few advantages worth discussing. In particular, for the wavelength tunability, and the future lighting technologies, the near-infrared (NIR) SSLs that exhibit considerable value in laser communication, optical storage, and optical information processing[73] have to be mentioned. Excited State Intramolecular Proton Transfer (ESIPT) compounds are a class of materials that have been investigated for use in SSL since they possess the ability to emit light when excited by an external energy source and can be easily incorporated into LEDs. These materials have unique properties, such as tunable emission wavelengths, high quantum yields, and good stability, which make them attractive for use in lighting applications as well as for fluorescent probes, biosensing, and bioimaging.[74,75] A very interesting example of organic crystals, showing their advantages such as low toxicity, and ease of processing is the silk protein that can be used for anticounterfeiting purposes.[76]

ESIPT-based materials can emit light at longer wavelengths due to the presence of an intramolecular hydrogen bond, which acts as a "proton shuttle" that facilitates the transfer of energy from the excited state to the lower energy state. Distinguishing the method described in ref. 77 single-crystal nanowire arrays exhibit remarkable characteristics due to the presence of

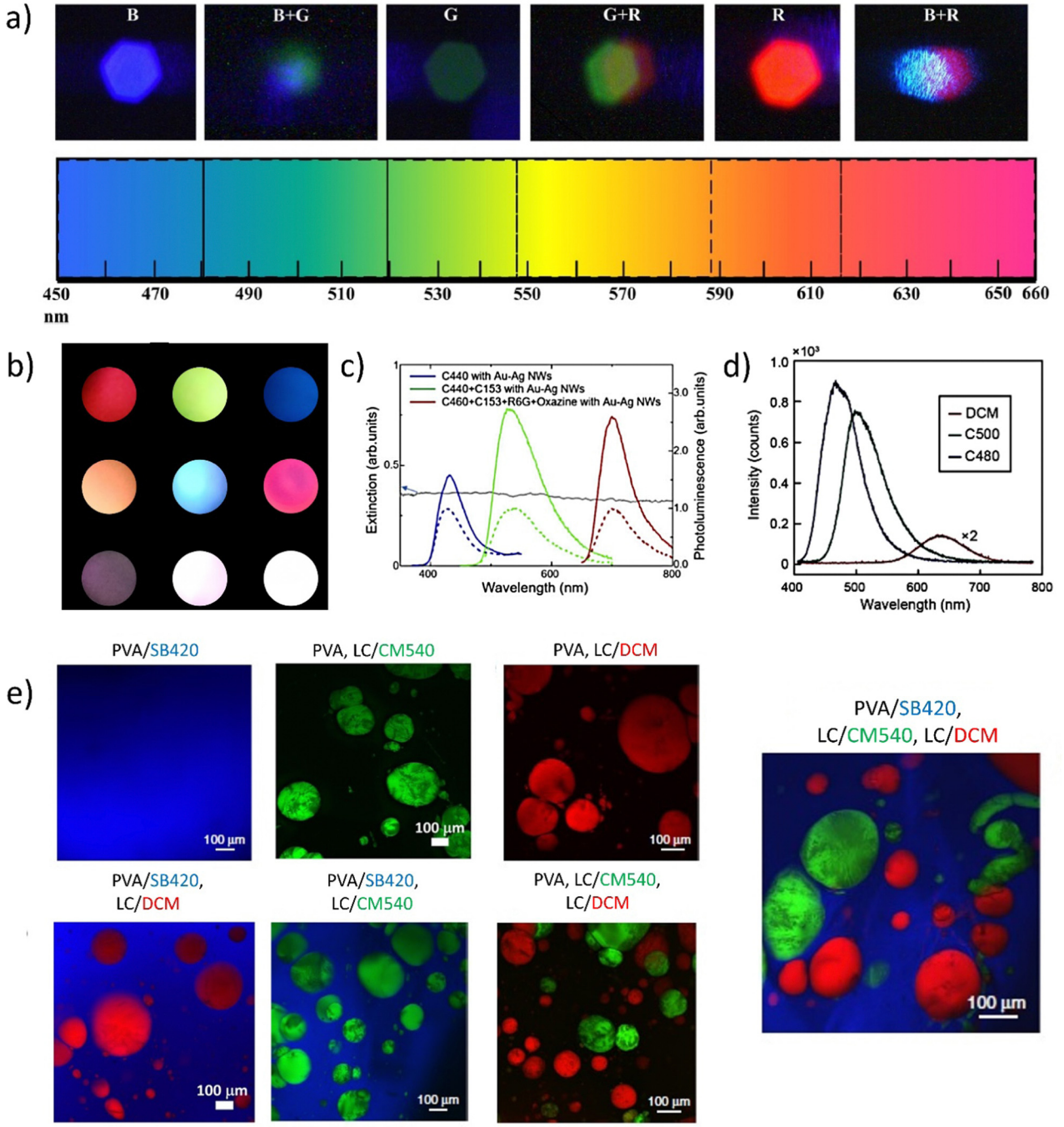

Fig. 6 Presentation of different strategies to obtain multicolor, tunable, and white lasing sources. (a) Color tuning with the use of SB420, CM 540, and R610. Reproduced (or Adapted) with permission,[67] 2019, APS. (b) Photographs of mixed far-field emission (used dyes are: DCJTB, R6G, SB420). The three top pictures present independent red, green, and blue lasers. Three central photographs are mixed colors coming from yellow, cyan, and magenta lasers. The bottom set of pictures shows the WRL, pumped below the (left image) threshold and above (central picture and the right). Reproduced under terms of the CC-BY license,[34] 2018, Springer Nature; (c) extinction spectrum of Au–Ag Nanowire (NW) suspension and photoluminescence spectra of C440 (blue), CM440 + CM153 (green), CM460 + CM6 + R6G + Oxazine (red) with Au–Ag NWs (solid) and without (dash) Au–Ag NWs. Reproduced (or Adapted) with permission,[40] 2020, OSA Publishing; (d) photoluminescence spectra of CM480, CM500, DCM dyes. Reproduced (or Adapted) with permission,[38] 2021, Wiley; (e) full-color tunability with the use of SB420, CM540, and DCM. The picture presenting PVA/SB420, LC/CM540, and LC/DCM system is responsible for white lasing. Reproduced under terms of the CC-BY license,[36] 2020, Springer Nature.

organic molecules that contain intramolecular hydrogen bonds. Under excitation, these molecules exhibit four electronic levels, including a normal form and tautomer, which result in a genuine four-level energy system that enables lasing action and red-shift emission without significant reabsorption. By tailoring the size of the organic nanowire arrays, it is possible to achieve

mode-tunable near-infrared lasing emission. These arrays, which are easily fabricated, can serve as active gain media and optical resonators simultaneously, thus enabling the realization of near-infrared lasers at the micro- and nanoscale and improving integrated optoelectronics based on organic materials. Another publication[78] describes the use of resonance-assisted hydrogen bonds (RAHBs) in ESIPT-active materials to prevent serious nonradiative decay during the ESIPT process, thereby facilitating their gain properties. The authors designed and synthesized an ESIPT-active molecule, DP-DHAQ, which exhibited a more than 30-fold higher photoluminescence quantum yield (PLQY) ($\approx$24.5%) and a 100-fold faster radiative decay rate attributed to the suppression of nonradiative-decays-by-RAHBs. Moreover, DP-DHAQ exhibited effective laser activity in both doped polystyrene (PS) microspheres and microcrystals. Both of them can be promisingly investigated for the creation of WLs. Therefore, it is presented that organic crystals are highly versatile and can be engineered to exhibit a wide range of optical properties. What is specifically important for this work, the advantages of organic crystals include also the possibility to obtain multicolor and white emission,[79–82] making them ideal candidates for a variety of laser applications.

For the discussion of organic crystals, it is worth taking an insight into the study presenting dibenzo[*g*,*p*]chrysene (DgpC)-based charge transfer (CT) complexes. They were employed to synthesize microwires composed of organic cores and shells. They are characterized by adjustable radial multicolor emission, and varying shell layer numbers through a simple horizontal epitaxial growth approach. For this goal, the blue-emissive DgpC, green-emissive DgpC-TFP (DgpC-tetrafluoroterephthalonitrile),

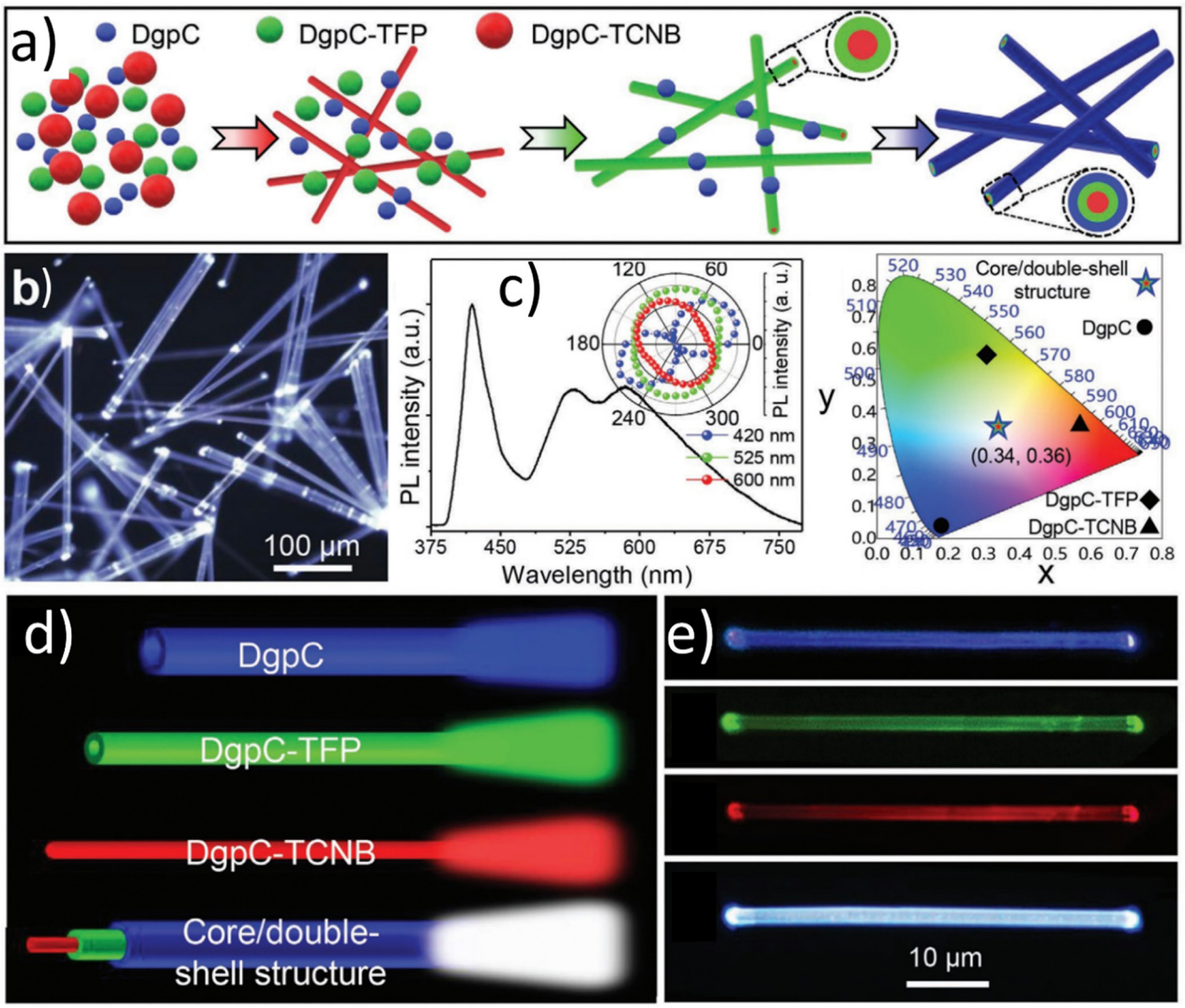

Fig. 7 (a) Schematic representation of the multiple horizontal epitaxial-growth process for the synthesis of the organic core/double-shell microwires. (b) FM image of DgpC-TCNB/DgpC-TFP/DgpC core/double-shell microwires with a scale bar of 100 μm. (c) PL spectra and CIE chromaticity diagram of DgpC-based core/shell microwires as shown in (b). Inset of (c): the corresponding polar image of the peak intensities. (d) Schematic representation of horizontal emission property in DgpC-TCNB/DgpC-TFP/DgpC core/double-shell microwires. (e) Laser confocal fluorescence microscopy (LCFM) images of an individual DgpC-TCNB/DgpC-TFP/DgpC core/double-shell microwire blue, green, red-emissive region and dual-emissive superposition region. Reproduced or adapted with permission from.[83]

and red-emissive DgpC-TCNB (DgpC-1,2,4,5-tetracyanobenzene) microwires were used. The progression of the horizontal epitaxial growth mechanism was governed by regulating the noncovalent interactions. The effect was observed on the matching desired lattice parameters. For example, DgpC-TCNB was found to exhibit robust red emission at 600 nm, DgpC-TFP microwires provided green emission at 525 nm, and DgC emitted a strong blue light color. Following this, multicolor microwires were purposefully generated, as outlined in Fig. 7a showing the white light emission (Fig. 7b).[83]

The PL spectrum of the DgpC-based core/multi-shell microwires reveals three distinct emission bands at 410 nm, 525 nm, and 600 nm, corresponding to the outer-shell, inter-shell, and core parts of DgpC, DgpC-TFP, and DgpC-TCNB, respectively (Fig. 7c). Notably, the CIE coordinates calculated from the spectra of DgpC, DgpC-TFP, and DgpC-TCNB are (x = 0.16, y = 0.04), (x = 0.30, y = 0.59), and (x = 0.58, y = 0.42), respectively, while the CIE coordinate calculated from the spectrum of the core/double-shell microwires is (x = 0.34, y = 0.36), which closely approaches ideal white-light (x = 0.33, y = 0.33). The WLE of the core/double-shell microwires is attributed to the recombination effect of the spatial emission of blue, green, and red light from the two hetero-shell layers and the core part (Fig. 7d). When excited with a 405 nm laser, spatial emission of blue, green, and red light along the radial direction is observed, as confirmed by laser confocal fluorescence microscopy (LCFM) images (Fig. 7f).[83]

2.4.5. Perovskites. Perovskites belong to a group of materials characterized by their particular crystalline structure and captivating photophysical properties such as high photoluminescence quantum efficiencies and a long carrier diffusion length. They are characterized by tunable bandgaps, allowing for control over the energy of the emitted photons. Moreover, they are known for light amplification.[84,85] The observed fluorescence color of perovskites is subject to several factors, such as chemical composition, crystal structure, and nanoparticle size. A noteworthy attribute of perovskites is their capacity to exhibit different light colors, which is commonly known as multicolor tunability. This exceptional trait stems from the fact that through the manipulation of perovskite composition and structure, it is feasible to regulate their band gap and thus the color of the resulting emitted light. In addition to their multicolor tunability, perovskites exhibit promising potential for white light emission.[86–89] This is primarily because white light generally comprises a blend of colors spanning the visible spectrum. By amalgamating different perovskite nanoparticles with diverse band gaps or sizes, it is possible to obtain a combination that emits light across the entire visible spectrum, leading to the WL or WRL. Perovskites are recognized as promising materials to realize novel, laser-based displays.[86,90] For example, methyl ammonium lead halide perovskites ($MAPbX_3$, X = Cl, Br, I, or their mixtures) possess advantageous traits such as prolonged balanced carrier transport, elevated optical gain, alterable bandgap, and straightforward solution processing. Therefore, they arise as a significant material category for fabricating state-of-the-art, laser-driven displays. Henceforth, it is important to establish an extensive methodology that enables swift expansion of perovskite electroluminescent microlaser arrays across extensive surface areas to realize portable displays. The example of realization of the novel wettability-guided screen-printing technique to enable the rapid and efficient production of large-scale multicolor perovskite microdisk arrays is presented in ref. 91 and demonstrated in Fig. 8.

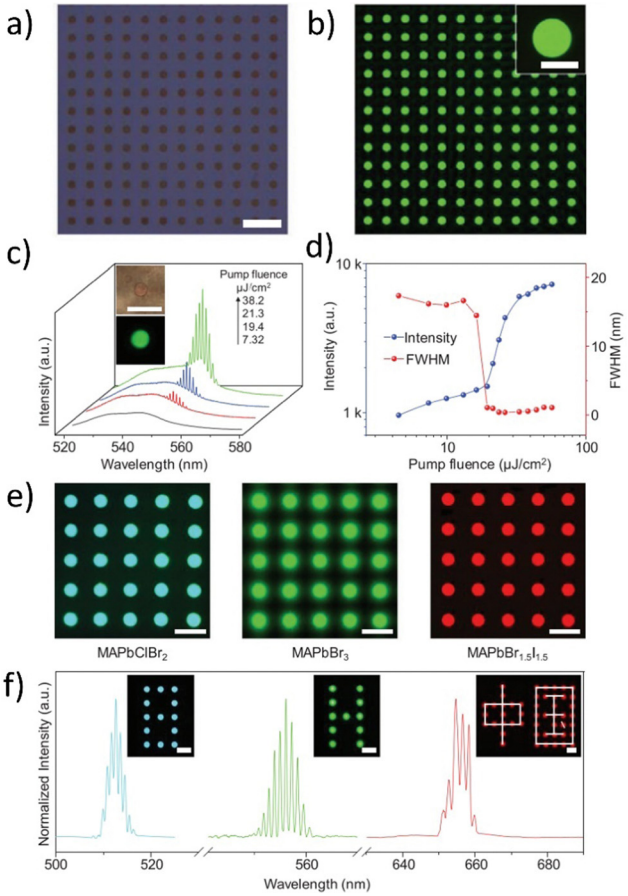

Fig. 8 (a) Bright-field, (b) PL images of an as-prepared $MAPbBr_3$ microdisk array; (c) PL spectra recorded from a typical $MAPbBr_3$ microdisk pumped with different energies. Insets are optical images of the same perovskite microdisk irradiated with white light (top) and a laser beam (bottom); (d) emission intensity and FWHM as a function of pump fluence; (e) PL images of multicolor perovskite microdisk arrays (from left to right are $MAPbClBr_2$, $MAPbBr_3$, and $MAPbBr_{1.5}I_{1.5}$) (f) widely tunable lasing from screen-printed perovskite microdisk arrays. The insets demonstrate a multicolor laser display showing different characters (cyan digit, green letter, and red Chinese characters). Scale bars, 50 μm. Reproduced or adapted with permission from.[91]

The authors utilized a few-steps wettability-guided screen-printing method to fabricate arrays of $MAPbX_3$ perovskite microdisks. They carefully controlled the crystal nucleation and growth to obtain large arrays of perovskite microdisks with a period of 50 μm (Fig. 8a) over various substrates using a lyophilic hole template. The resulting perovskite microdisk arrays emitted bright and uniform green light (see Fig. 8b). Optical images and corresponding emission spectra of an isolated $MAPbBr_3$ microdisk were obtained by exciting it with increasing laser power. At a low pump fluence, the perovskite polycrystalline microdisk exhibited broad spontaneous emission, while at a

higher pump fluence, the emission spectrum contained a set of sharp peaks centered at ≈551 nm, indicating the occurrence of stimulated emission (see Fig. 8c). The PL intensities plotted against the pump fluences exhibited an S-shaped nonlinear behavior, demonstrating the transition from spontaneous emission to full-lasing oscillation. The occurrence of lasing was confirmed also by the sharp shortening of the PL lifetime which is discussed in ref. 91. For the FWHM (Full-Width-At-Half-Maximum) parameter, there is the possibility to observe drastic narrowing from 17.4 to 0.35 nm and this verifies the high-quality factor (Q, defined as λ/FWHM) of ≈1570 for the obtained system (see Fig. 8d). The well-defined circular boundaries and emission covering the blue to near-infrared region demonstrated the universality of the screen-printing method for perovskite materials. As-prepared perovskite microdisks with different halide anions (from left to right are $MAPbClBr_2$, $MAPbBr_3$, and $MAPbBr_{1.5}I_{1.5}$) exhibited tunable lasing wavelengths ranging from ≈510 nm to ≈650 nm and could be used as laser pixels to construct color display panels with different characters (Cyan digits, green letters, and red Chinese characters) which were displayed in the inset in Fig. 3d. The prepared perovskite-based multicolor system is characterized by similar lasing intensities, outstanding reproducibility, and almost identical lasing modes among different microdisks. These properties make them practicable and very appealing for simultaneous lasing as individual pixels for display panels. Therefore, should be concerned as the promising candidates for WL.

Our discussion on materials for white and multicolor lasing is summarized in Table 1. It demonstrates all the key features of QDs, LCs, luminescent dyes, organic crystals, and perovskites. The central objective was to establish a correlation between distinct materials and the fundamental properties required for the production of white laser light. The table exemplifies the diverse laser mechanisms that have been realized through the use of a variety of compounds. Furthermore, it provides a detailed comparative analysis of the advantages and drawbacks of the materials. An essential aspect highlighted by the table is the distinct role that each material plays in the white lasing achievement. With contemporary technological advancements, the capacity to modulate the resulting color of emission is critical. In light of this, the final column of the table delineates the strategic approaches that can be employed for each material group to achieve the desired color tuning.

3. White lasing and ASE

Optoelectronic devices based on inorganic materials were widely used in the XXth century. For the White Light Spontaneous Emission, it is worth mentioning LEDs. Most of the LEDs which emit white light are blue diodes. The chosen luminophore converts the blue color to white and it generates main disadvantages like redundant losses translating into worse efficiency of the white light. Some weak luminophores may tend to change their color from white to yellow/blue or burn out quickly. Organic materials have made a comeback as innovative optically active layers in the 21st century. As opposed to disadvantages, their benefits started to be seen as being increasingly prevalent. To reduce the drawbacks of organic materials, such as their low stability in ambient circumstances

Table 1 A comparison and summary between QDs, LCs, luminescent dyes, organic crystals, and perovskites

Material	Lasing mechanisms examples	Advantages	Disadvantages	Role in WRL/WLE	Multicolor tunability strategies
Quantum dots	WGM,[92,93] RL,[16,94,95] ASE[96]	High efficiency Narrow emission linewidth Provides many emission colors Compatible with different substrates	Limited stability – Toxicity concerns	Used as up-conversion material to generate white light	Size and composition tuning
Liquid crystals	RL,[38,97] WGM,[98,99] DFB,[100–102] ASE[103]	Low threshold – Tunable Fast response time Can be electrically or optically addressed Can be luminescent itself	Limited stability Occurring in the particular temperature ranges	Used as a host material for luminescent dyes in white light generation	Guest–host systems, doping with dyes or quantum dots
Luminescent dyes	RL,[104] DFB,[105] WGM,[106] ASE[105]	Wide color range Low cost Easy to fabricate and modify High gain	Limited stability – Short lifetime Photobleaching – Potential toxicity	Used as active materials providing gain in white light lasers	Chemical modifications, doping with other dyes or nanoparticles
Organic crystals	DFB,[100,107] RL,[108,109] WGM[110]	High efficiency Tunable Low operating voltage Compatibility with flexible substrates	Limited stability – Relatively high cost Difficult to fabricate	Used as a color conversion material or active material	Molecular design, doping with other materials
Perovskites	RL,[85,111,112] DFB,[113] WGM[114,115]	High efficiency Tunable Low cost Compatibility with flexible substrates Large absorption cross-section Solution-processable	Limited stability Toxicity concerns Degradation under moisture and heat Limited commercial availability Not all of them provide light amplification	Used as active materials or matrices	Composition and morphology tuning, doping with other materials

and, as a result, their short operating times, new projects and optimization methods have been undertaken. Organic materials have peculiar qualities like the ability to modify their chemical structures readily and the simplicity of integrating them into systems, as well as comparatively low costs, great flexibility, and environmental friendliness.

In the last years, increasing interest in searching the fully organic WLE, WL, and WRL sources is observed. Currently, the most popular white-light emitters are LEDs and OLEDs. The main difference between them is that OLEDs are manufactured using organic semiconductors, while LEDs are embedded in crystals derived from inorganic materials. There are also noticeable differences between the two types of semiconductor lighting: LEDs are flickering points of light, while OLEDs are thin, flat panels that emit light evenly over the entire surface. The light they produce is diffused and friendly for the human eyes. OLEDs cannot be considered as the replacement for LEDs since both technologies have very specific and practical types of applications. OLED and LED-based systems can complement each other providing many varied possibilities in the era of digital lighting.

On behalf of this short discussion of past and current technologies, it is worth taking an insight into lasers as the source of light for imaging, sensing, lighting, biomedical and other applications, as the future technology. In this work, the main goal is to present the different approaches, concerned with white lasing with the help of inorganic, organic, and hybrid materials.

3.1. Inorganic

The discovery and construction of the semiconductor, the first white laser[116] in 2015 proved that laser light can offer more than only one wavelength of emission and this was a major breakthrough. A widely emphasized feature of a typical laser is that it emits light in one color, with a specific wavelength. The creation of a laser that emits white light, composed of the three primary colors, was an extremely demanding discovery. The device relies on the multi-segment heterostructure nanosheets obtained by chemical vapor deposition (CVD). For this purpose, individual monolithic ZnCdSSe nanosheets[117] have been used. To finally obtain this structure, the authors altered the growth circumstances and sequencing such that the CdSe nanosheet growth was followed by a dual-ion exchange reaction, a previously unreported process. The realization of multi-segment heterostructure nanosheets (MSHNs) that enable simultaneous RGB lasing depends on this development method. In Fig. 9a, the main part of the multi-color cavity (marked as the white bracket) is presented.

The middle photograph shows luminescence and all of the colorful RGB components can be recognized. Fig. 9b depicts the spectrum evolution as the pulse energy increases. Only broadband spontaneous emission is seen at the lowest pumping energy of 1.3 mJ. Narrow peaks in the colors red (642 nm and 675 nm), green (530 nm), and blue (484 nm) consecutively appear as the pumping energy is increased from 1.8 mJ to 3.3 mJ. Due to the well-known multimode lasing behavior, both the intensity and the number of peaks of each color grow with the increase of the pumping energy. The authors explored the dynamic tuning of the mixed colors in the full-color spectrum, and white color lasing in particular, to show the potential of the MSHNs for general lighting. To pump one of the three segments, each of the three beams was focused into a long, narrow, parallel stripe. It was possible to precisely tune the intensity of each color's lasing by independently adjusting the power of the particular pumping beam. The desired white light can then be obtained by controllably varying the mixed lasing colors in the far field across the complete color spectrum. The real color images of the laser output were acquired and demonstrated in Fig. 9c. The modulation of the lasing color was

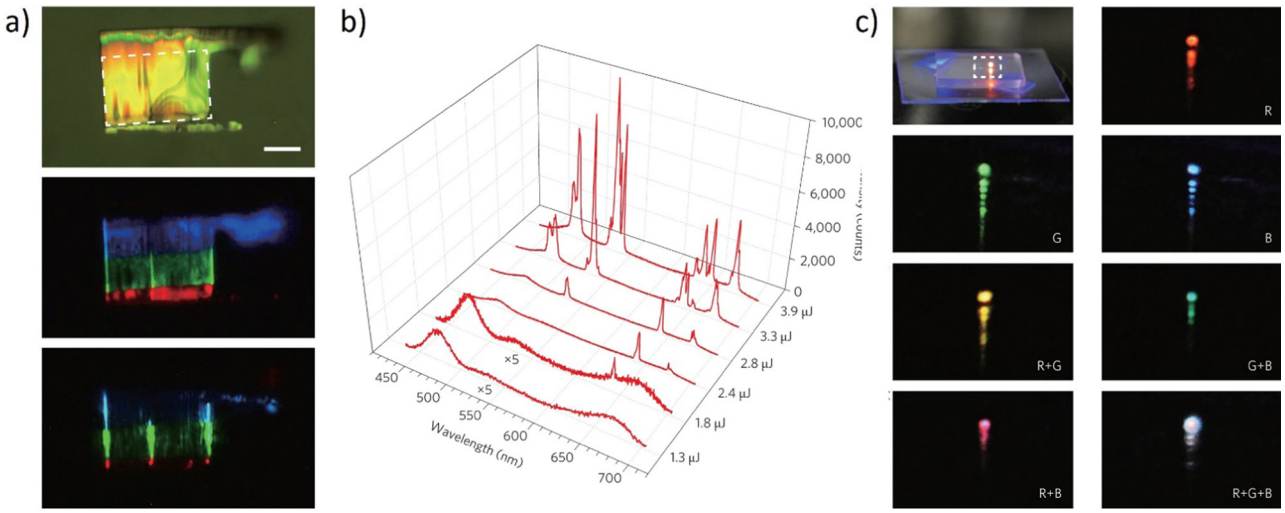

Fig. 9 (a) Bright-field optical microscope image (Scale bar, 10 μm). The three strong vertical lines indicate significant scattering from the two edges and the bent edge in the center; (b) spectra at different pumping levels (as labeled on the lower right side of the figure). The intensities of the first two spectra have been multiplied by a factor of 5 to show the details; (c) photograph of the mixed emission color from a multi-segment heterostructure nanosheet. Photographs of the enlarged dashed-box region, when the different combinations of segments are pumped as indicated by the labels inside each figure, create the mixed far-field emission colors red, green, blue, yellow, cyan, magenta, and white. Reproduced (or Adapted) with permission.[116] 2015, Springer Nature.

utilized, to demonstrate the far-field mixing of colors from the multi-color lasers (red, green, and blue). Pumping two of the segments resulted in the creation of mixed lasing emissions in cyan, magenta, and yellow, as illustrated in Fig. 7c. Finally, simultaneous RGB lasing from the single MSHN can be combined to portray a white color, when three beams pump all three color segments. To conclude, the authors' findings show that the seemingly incompatible concepts of both "white" and "lasing" may be realized in a single monolithic structure, opening the door for the development of more new applications.

Another example of the inorganic system dedicated to white random lasing emission is based on the $NaYF_4$:Yb/Er/Tm@ $NaYF_4$:Eu core–shell nanoparticles deposited on the top of the Au/MoO_3 multilayer HMM (Hyperbolic Meta-Material).[62] The idea is based on the Random Lasing (RL) mechanism which possesses a significant advantage over conventional lasers due to their inexpensive manufacture and streamlined fabrication procedures.[118–120] Commercialization of WRL can bring many benefits, which are discussed further, in the section "Applications and perspectives". HMM is a type of optoelectronic device made of well-aligned metal nanowires inserted inside a dielectric medium or alternatively organized metal and dielectric layers of the right composition and the choice of these materials is supported by the high scientific interest.[121–123] One segment of a white random laser can be produced by core–shell nanoparticles as it is presented in Fig. 10a. The UCNP (up-conversion Nanoparticles) clusters' porous structure serves as a microcavity for photon scattering, which produces the optical feedback gain for the released light.

By utilizing the spin-coating technique, the as-synthesized UCNPs were coated on HMM 1, HMM 2, HMM 3, and SiO_2/Si substrates with a thickness of 200 nm. Fig. 10b depicts a typical device with a UCNP layer thickness of 500 nm or less, attained at a 2000 rpm spinning speed. It is interesting to note that the very porous structure of the sample makes it possible to create coherent feedback closed loops for the photons that the UCNPs release by inducing numerous scatterings. In Fig. 10c, the emission spectra are presented, which are calculated into the CIE XYZ plot. The authors developed the devices using three different HMM samples, as mentioned earlier, to show how the upconversion emission (UCE) was enhanced. All of the UCE spectra were taken on various substrates and the reference sample while maintaining a constant pump power density. It is interesting to note that how the emission spectra drastically varied for different substrates. It was found that the upconversion emission factor for HMM 1 can reach values of more than 50 times. For the red and green lines, respectively, HMM 2 can help with a strong enhancement of 50 and 30 times. The transition lines in the visible range, however, can only be improved by about 10 times using HMM 3. By computing the Commission Internationale d'Eclairage (CIE) coordinates corresponding to the emission spectra as shown in Fig. 8d, the variance of the color produced by the miscellaneous devices has been estimated. It is evident that the HMM 1 sample's CIE index (0.333, 0.334) closely corresponds to the white light emission region. The greatest value yet reported, the observed laser action spans a broad spectral range of more than 200 nm. The authors' demonstration is enabled by a set of significant elements. When driving lasing action by the amplification of radiative transition, the presence of a strong high photonic density of states (PDOS) from the HMM substrates is particularly helpful. With this straightforward architecture, the emission improvement of upconversion >50 times is exciting and demonstrates significant potential for practical applications. Additionally, it causes the lasing threshold to be drastically reduced.

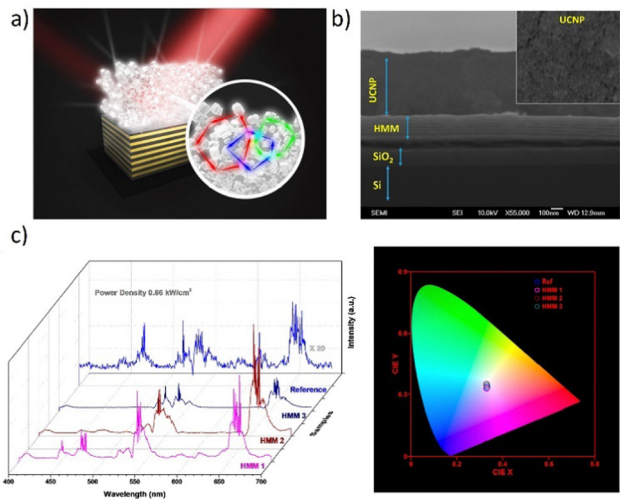

Fig. 10 (a) A white light emitting device – schematical structure; (b) cross-sectional SEM image of the composite heterostructure. The inset shows the top view of the UCNP, which shows the porous structure of the sample. Hyperbolic metamaterial induced enhancement of up-conversion emission. (c) Emission spectra from UCNP/HMM composites under the excitation of 980 nm laser at a constant pumping power density of 0.66 kW cm^{-2} and the corresponding plot of the calculated CIE coordinates (reference, (0.332, 0.331); HMM 1, (0.333, 0.334); HMM 2, (0.334, 0.354); HMM 3, (0.334, 0.342)). Reproduced (or Adapted) with permission.[62] 2018, ACS.

Discussing the inorganic white lasers, it is worth mentioning the Quantum Dots (QDs), combined with the very interesting class of two-dimensional inorganic compounds.[16] Several articles present an emerging family of 2D nanomaterials, labeled MXenes.[16,124–127] It has been developed by selectively etching MAX phases, where M represents an early transition metal, A represents the main group of 3 or 4 elements, and X is either carbon or nitrogen. They possess outstanding chemical, physical, and environmental properties that distinguish them from traditional 2D materials, such as high metallic electronic conductivity, the ability to produce transparent conductive films, excellent chemical stability, and environmental friendliness. According to their limited photoluminescence, the authors decided to utilize the hybrid system by connecting the Vanadium Carbide V_2C (MXene) and the QDs' outstanding properties.[16] The strategy was to control the passivation process to enhance the photoluminescence of the MQD.[128,129] Given that MXene materials contain at least three atom layers due to their distinctive structural properties, the V_2C MQDs with the fewest layers should have improved and widened photoluminescence after passivation. As a result, the spectra tuning covered the entire visible light range. A huge role in the experiment was played by the nonlinear scattering, controlled by the optimization of colloid concentration.

Fig. 11a presents the appearing of two peaks with centers placed at 545 and 613 nm as the pumping fluence increased. This effect could be explained by nonlinear scattering with reabsorption and reemission. The scattering effect became more apparent as the pump beam energy fluence increased, resulting in increased light diffusion length, which accompanied the increased reabsorption at the shorter wavelength and resulted in re-emission at the redshift.

Fig. 11b demonstrates the lasing thresholds at various wavelengths (1.6 mJ cm^2 at 490 nm, 0.4 mJ cm^2 at 545 nm, 0.88 mJ cm^2 at 587 nm, and 0.64 mJ cm^2 at 613 nm), as well as the relationship of the spectral peak intensity and the related linewidth in the function of pumping energy fluences. The linewidth becomes practically unchanged under high pump energy fluences (14 nm at 490 nm, 9 nm at 545 nm, 13 nm at 587 nm, and 7 nm at 613 nm). There can be noticed that the intensity almost linearly increases with the pump energy fluences, which is typical for lasing. The white laser was observed with a pumping fluence of 4.8 mJ cm^2 (Fig. 11d). Fig. 11c depicts the evolution of chromaticity as a function of pumping fluence. On the CIE 1931 color map, the six points corresponding to the spectra presented in Fig. 11a reflected the predicted chromaticity of emission spectra under various pumping fluences. With increasing pumping fluence, the

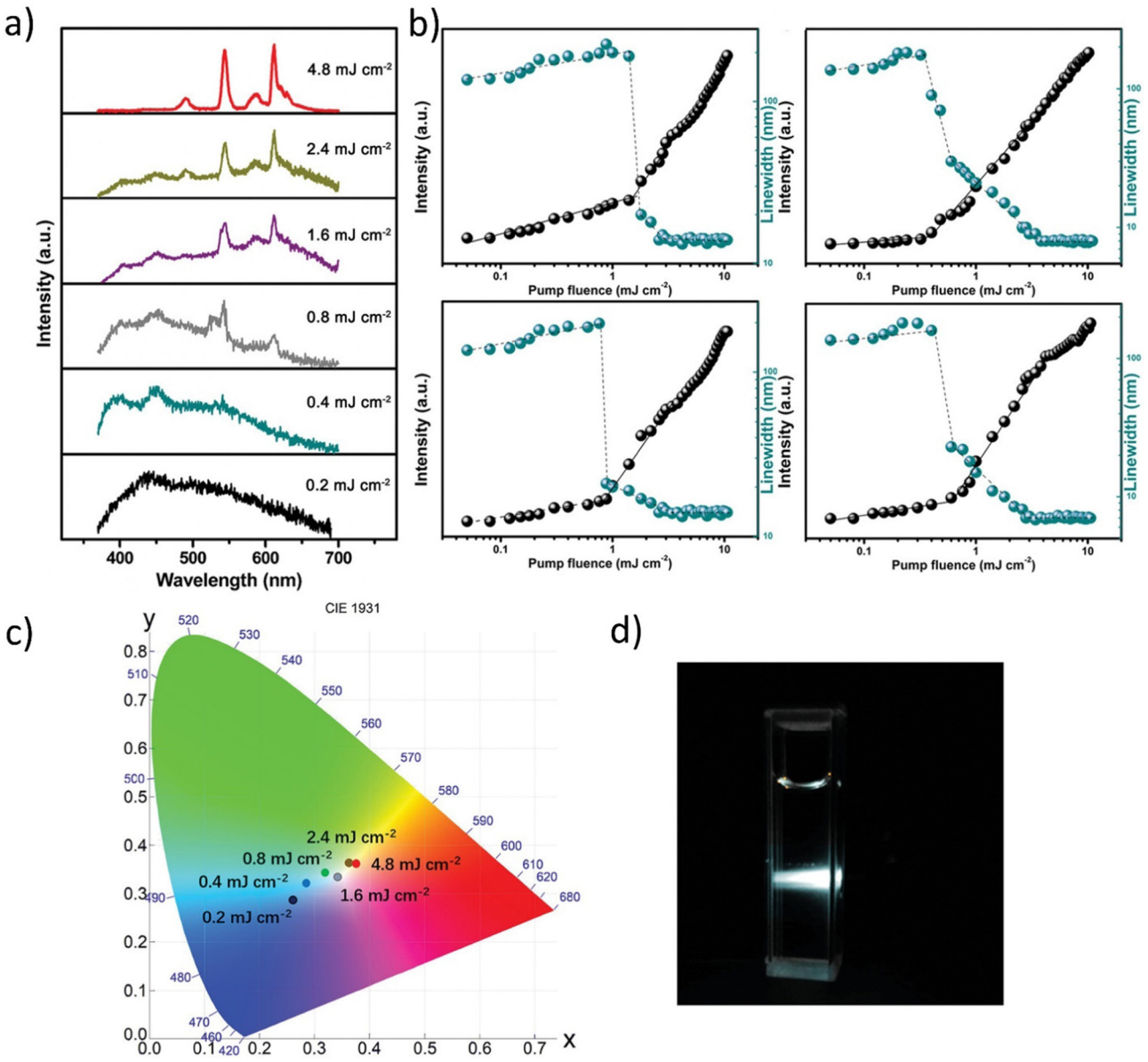

Fig. 11 (a) Emission spectra from the V_2C MQD colloid for different pump fluences. (b) Dependence of peak intensity and linewidth of the dominant emission peaks plotted as a function of pump fluences shows the lasing threshold behavior. (c) The plot of the calculated CIE coordinates of emission spectra under different pumping fluence (0.2 mJ cm^{-2} (0.269, 0.294); 0.4 mJ cm^{-2} (0.296, 0.325); 0.8 mJ cm^{-2} (0.329, 0.34); 1.6 mJ cm^{-2} (0.349, 0.334); 2.4 mJ cm^{-2} (0.373, 0.365); 4.8 mJ cm^{-2} (0.383, 0.365)). (d) Photos of the operating V_2C MQDs colloid under 355 nm pulsed laser pumping at 4.8 mJ cm^{-2}. Reproduced or Adapted with permission.[16] 2019, Wiley.

chromaticity of the MQDs colloid shifted from blue (the CIE XYZ coordinates: 0.269, 0.294), neutral white (0.349, 0.334), to warm white (0.383, 0.365), implying that white emission is achieved through a dynamical balance between each color gain. The concentration of the ions can be varied which results in the emission and allows for its effective tunability. Therefore, under NIR stimulation, a single hexagonal microrod can produce WLE based on the three primary colors on the Whispering Gallery Wave (WGW). Fig. 12a plots the radius, R, of the 40 percent Yb^{3+}, 2 percent Tm^{3+}, and 0.5 percent Er^{3+} tridoped –$NaYF_4$ hexagonal microrods under 980 nm ns-pulsed excitation against the energy density thresholds of the RGB lasing modes (at 654, 540, and 450 nm). It has been noted that when R increases, the threshold difference between the RGB lasing modes gets less. Therefore, it is preferable to choose a value of R = 4 to enable simultaneous excitation of the RGB lasing modes and to preserve stable single-mode lasing.

The light-light curves of the tridoped $NaYF_4$ microrod with a 40 percent Yb^{3+}, a 2 percent Tm^{3+}, and a 0.5 percent Er^{3+} content are plotted in Fig. 10b with R equal to 4 mm for the RGB modes. A 980 nm ns-pulsed laser was used to stimulate the microrod at room temperature. Fig. 12c demonstrates the microrod's associated lasing spectra for pumped power densities of 1.0 and 21.6 mJ cm^{-2}. The sample's microscope image is shown in the inset. The system is maintaining single-mode lasing emission at wavelengths of 654, 540, and 450 nm. Additionally, white-light lasing can be seen on the hexagonal microrod's flat surface; for more information, see Fig. 12c's inset. For the RGB lasing modes, Fig. 12d depicts the corresponding emission linewidth *vs.* pumped power density. Fig. 12b to d illustrates a bend in the light-light curves as well as the concomitant narrowing of emission spectra from the RGB laser modes. The detection of blue, green, and red lasing emission suggests that the microrod enables white-light lasing because these are the fundamental

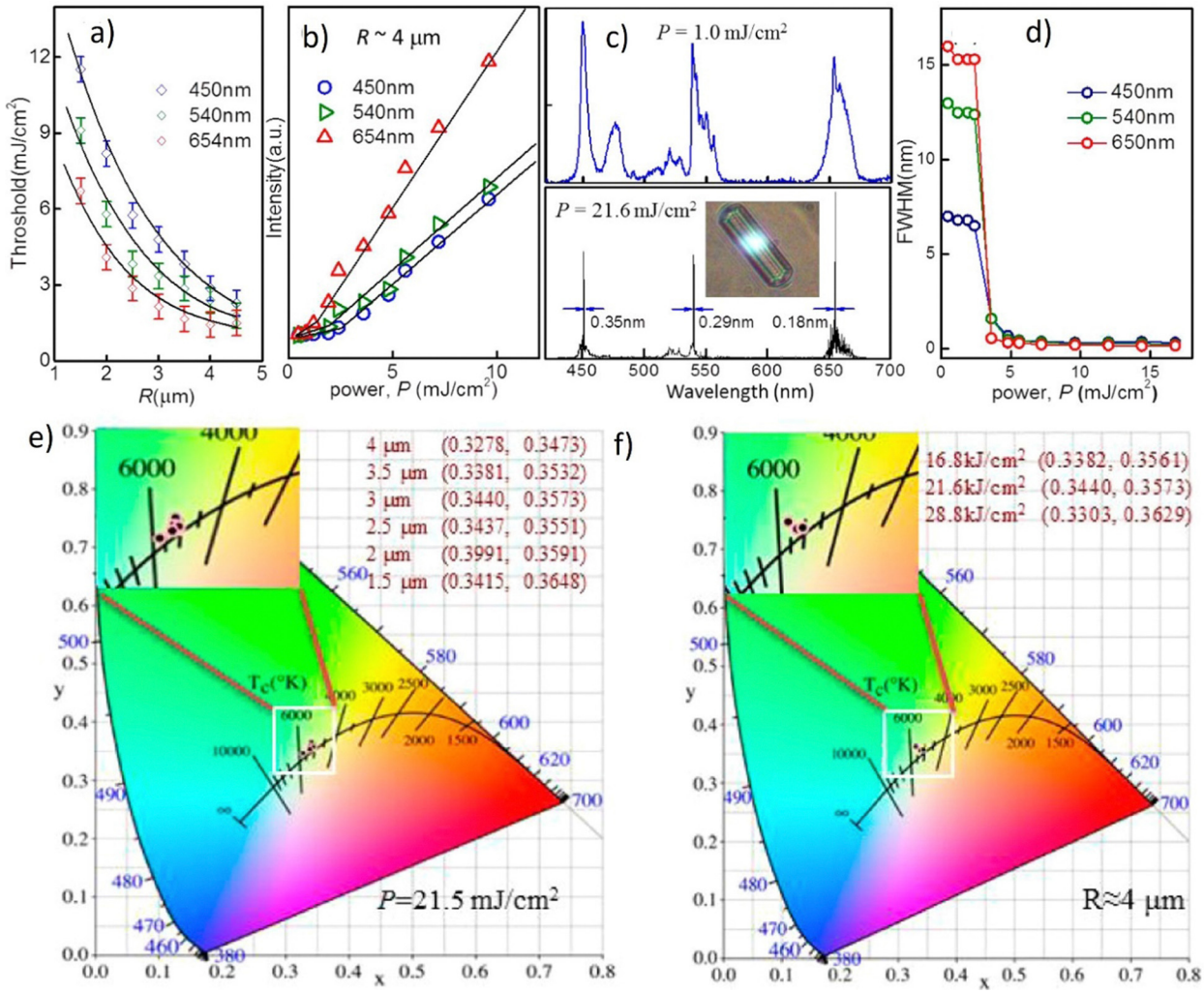

Fig. 12 (a) Plots of the threshold, P^{th}, *versus* radius, R, of the doped β-$NaYF_4$ hexagonal microrods with λ equal to 654, 540, and 450 nm. (b) Light–light curves, (c) emission spectra and (d) lasing linewidth of the RGB modes for a 40% Yb^{3+}–2% Tm^{3+}–0.5% Er^{3+} tridoping microrod with R equal to 4 μm. The inset in (c) shows the corresponding microscopy image under 980 nm ns-pulsed excitation at room temperature. (e) Plot of CIE1931 color coordinates of the doped microrods under lasing emission with different R with pumped power kept at 21.5 mJ cm^{-2} and (f) pumped power with R kept at 4 μm. Reproduced (or Adapted) with permission.[32] 2017, ACS.

colors of white light. The calculated coordinates (Fig. 12e and f) for the equivalent CIE 1931 color diagram with different values of R (with P = 21.5 mJ cm^{-2}) and P (with R = 4 μm), respectively, are namely: x = 0.3440 and y = 0.3573. The white point for CIE standard illuminant coordinates is described as x = 0.33 and y = 0.33. Therefore, it can be concluded that these experimental values are extremely near to the benchmark ones.

3.2. Hybrid organic–inorganic

This study involves the design, fabrication, and demonstration of the WRL with on-chip integration based on three monochromatic organic laser dyes. Organic technology is being introduced into optoelectronics according to indisputable advantages such as low material cost, all-solution method, thin layer coating, self-assembly morphology, *etc.*[130–132] A further incentive for researchers to use organic materials in various domains is the extraordinary commercial success of OLEDs or organic solar cells.[132–136] The authors have taken use of low-cost, solution-based, and self-assembled methods to create RGB monochromatic polymer films (MPFs) for the WRL emission. The whole device relies on the utilization of organic and inorganic materials: Micro-porous films, MPFs, with disordered DCJTB (red organic dye) and blue (Stilbene 420) nanoparticles. Instead, the green-MPF is embedded with self-assembled silver nanoparticles (Ag NPs) as plasmonic scattering centers. The green color is provided by the Rhodamine 6G. The sample is optically pumped by a 266 nm pulsed laser. Fig. 13a demonstrates the emission intensities at various pumping energy.

Under the pumping energy of 8.2 mJ cm^{-2}, broadband spontaneous emission is noticed. Three protruding emission bands with superlinearly enhanced intensity, centered at roughly 620 nm, 562 nm, and 465 nm, were observed by increasing the pumping energy density from 8.2 mJ cm^{-2} to 10.7 mJ cm^{-2}. The light-in-light-out curves (Fig. 13c) exhibit superlinear changes from the regime of spontaneous emission to the regime of STE, providing strong support for the existence of the RL phenomenon. The CIE chromaticity diagram (Fig. 13b) displays five points, each of which represents the RL's chromaticity at various intensities of recorded spectra. All of the points are located closer to one another in the white region. When the pumping intensities increase, the chromaticity of WRL remains practically fixed which implies that the white emission is extremely stable and almost chromaticity-unchanged at various pumping settings. This feature is worth underlining since it is crucial for a variety of illuminant applications. Fig. 13d shows the color-tunability of WRL. The contribution of spontaneous emission is subtracted using the Lorentz fitting method to determine the chromaticity of individual and mixed random lasing. This procedure allows for a more precise calculation of the composite color resulting solely from the lasing contribution. Fig. 13d shows the spectra for individual RGB random lasing, two-color lasing mixing, and simultaneous three-color RL. As a result, a wide range of colors can be achieved by varying the proportions of each distinct RGB emission when adjusting the far-field lasing color. On a CIE 1931 color chart, Fig. 13e displays the computed chromaticity of these spectra. It is demonstrated that the triangle zone formed by the three-elemental lasing colors in the diagram spans a wide range. Therefore, based on Grassmann's law, color-tunable RL can be accomplished within this triangular gamut by properly combining the three elemental lasers. The balanced three-color random

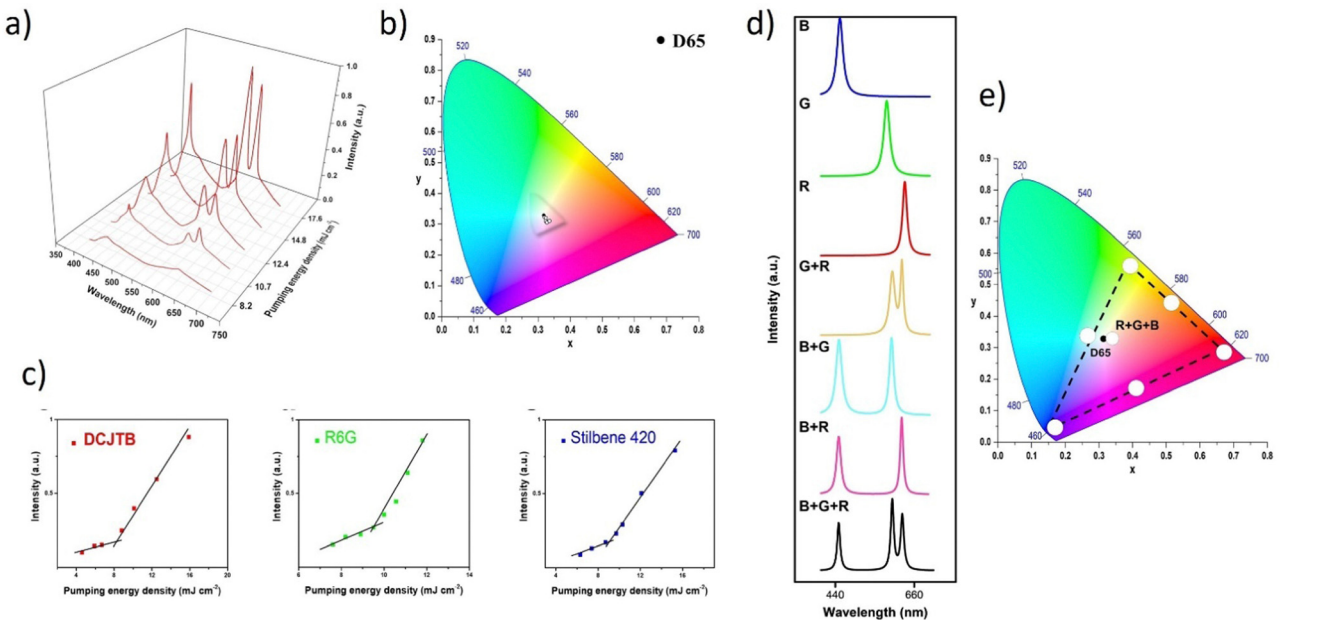

Fig. 13 Multi-color random laser under different pumping levels; (a) multi-wavelength lasing spectra at different pumping levels (b) chromaticity of the emission spectra; (c) evolution of emission peak intensity as a function of pumping energy density of red, green, and blue (monochromatic laser films. (d) White and full-color tunable random laser; lasing spectra of blue (B), green (G), red (R), red and green (R + G), green and blue (G + B), red and blue (R + B) and red, green, and blue (R + G + B) laser films; (e) tunable chromaticity of the lasing spectra extracted from the spectra in (d). Reproduced under terms of the CC-BY license.[36] 2018, Springer Nature.

lasers' color is also quite similar to the CIE 1931 diagram's reference white point. By merging RGB MFPs on a single chip, this result allows us to fully realize White-RL.

Another example of WRL is presented in the Optics Express.[42] Authors investigate the broadband-enhancement Au–Ag nanowires as scatterers. On the way of the resonance energy transfer (RET) between three chosen, organic dyes in the capillary microfluidic channel, the coherent WRL with controllable chromaticity can be achieved. The Au–Ag nanowires are promising for realizing this idea, according to their rough porous structure, wideband plasmonic resonance properties, and the fact, that the scatterers for the RGB multicolor random laser can significantly enhance the electromagnetic field. It is well known that the nanogap within the dimer of gold nanoparticles (NPs) has the potential to increase the fluorescence intensity hundreds of times.[137–140] Additionally, the emission band of the gain materials has to show a good overlap with the plasmonic resonance band. As a result, the scatterers for the multi-color random laser should have broadband plasmonic resonance spectra throughout the whole visible spectrum. The plasmonic resonance of the nanogaps and/or nanotips with random distribution and sizes within Au–Ag nanowires, as well as the favorable optical feedback provided by the capillary wall, is used to individually manufacture RGB RL, characterized by the low thresholds. The color adjustment and coupling of the three primary-color laser sit are possible to achieve WRL.

Fig. 14a demonstrates the details of the WRL-emitting system.

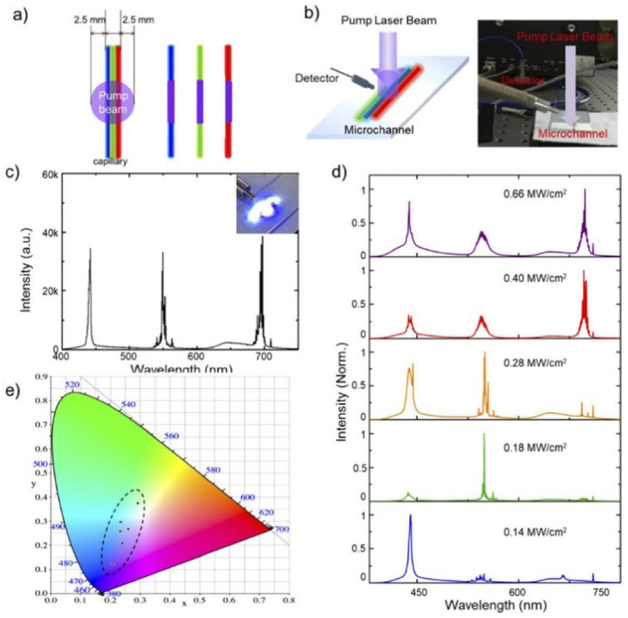

Fig. 14 (a) Assembly details of the WRL; (b) schematic diagram (left) and photograph (right) of the setup for white random laser; (c) lasing spectrum from random systems excited by 355 nm pulses at the pump power density of 0.82 MW cm^{-2}. Insets: Photograph of the exciting white random laser; (d) normalized multi-color lasing spectrum from the integrated random systems excited by 355 nm pulses under different pump power densities; (e) chromaticity of emission lasing in (c) and (d) as six black dots. Reproduced (or Adapted) with permission.[42] 2020, OSA Publishing.

Fig. 14a depicts the integration of adjacent R-G-B trichromatism random lasers on a substrate. The pulsed laser, set for 355 nm, was used to pump the sample, as seen in Fig. 14b. The green and red RLs are further cascade-excited by the blue RL, which is positioned in the center. By evenly coupling the RGB lasing as illustrated in Fig. 14c, the WRL is achieved when the pump power density reaches 0.82 MW cm^{-2}. The associated picture is shown as the right inset of Fig. 14c and demonstrates a brilliant white light coming from the microfluidic channels. The energy distribution of the RGB three-color spectrum may be gradually modified by adjusting the pump power density. As the pumping power density rises from 0.14 MW cm^{-2} to 0.66 MW cm^{-2}, the intensity ratio between the three emission bands visually changes (Fig. 14d). The intensity of the three-color RL exhibits a non-linear growth when the pump power density is raised above 0.28 MW cm^{-2}, which may be attributed to the coupling and competition mechanism between the various color RLs. Thus, altering the pump power densities might be used to adjust the chromaticity of obtained WRL. The points in the CIE 1931 color diagram in Fig. 14e represent the chromaticity progression of the emission spectra demonstrated in Fig. 14c and d. It underlines how a wide spectral range is covered by the coherent RL combined with RGB emission. As a result, with various pump power densities, the WRL with chromaticity control is possible.

For the hybrid organic–inorganic system, it is worth mentioning one of the most interesting, novel concepts reported in Advanced Materials in 2021.[40] The presented idea is supporting the advantages of hybrid organic–inorganic systems investigation towards multicolor and white lasing. First of all, the laser sources offer high-purity monochromatic colors and can extend the color range up to 78%.[141] What's more, surface lattice resonances (SLRs) may easily have their wavelengths changed by manipulating the lattice parameters according to the fact that they are hybrid modes made of localized surface plasmons (LSP) connected to Bragg diffraction modes.[142] By combining these materials, it is possible to obtain multiwavelength emission. A plasmonic white laser was realized by mixing the commercially available dyes (DCM, CM 480, and CM 500) in a solution sandwiched between the NP lattices in the form of squares (Fig. 15a). These specific laser dyes were selected as gain materials to achieve lasing emission from NP cavities because their photoluminescence spectrally overlaps with the desired RGB SLR modes. Solvent-assisted nanoscale embossing (SANE) and PEEL (a method combining phase-shifting photolithography, etching, electron-beam deposition, and lift-off)[143,144] were employed to create two 2D square arrays of Al NPs on fused silica spanning cm^2-areas, resulting in the fabrication of nanocavities with SLR modes at the required wavelengths. Fig. 15b presents the transmission spectra of the lattices, together with the individual dye lasing spectra.[40]

On the CIE XYZ chromaticity triangle, it is possible to see the simultaneous blue and red lasing emission (marked as BR1, BR2, and BR3) from a mixture of C480 and DCM dyes Fig. 15c. The human eye views this color mixture as magenta. On the other two sides of the triangle, the concurrent green-red lasing (GR1, GR2, GR3) and green-blue lasing (BG1, BG2, BG3) are

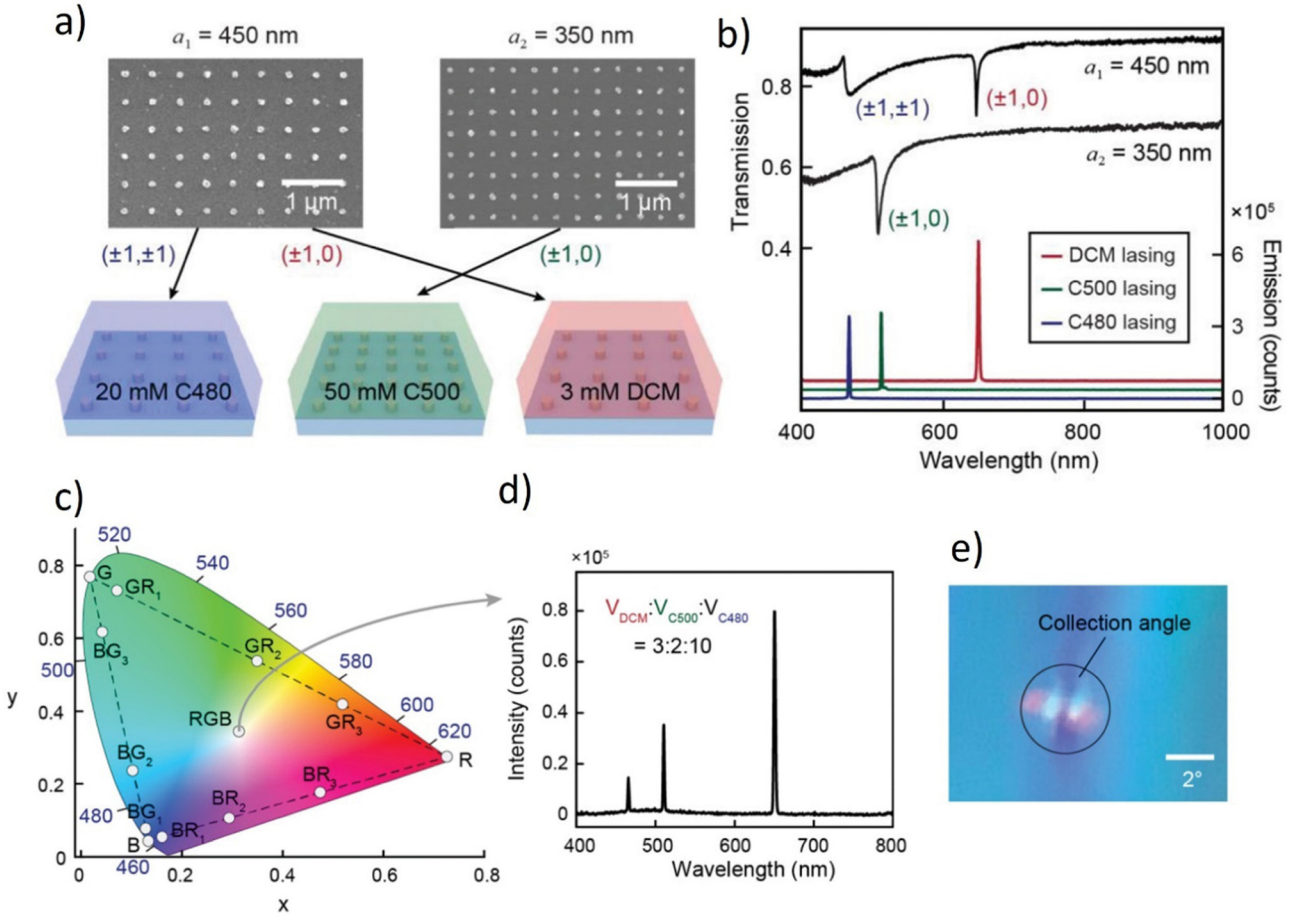

Fig. 15 Blue, green, and red lasing from two plasmonic nanoparticle lattices. (a) Scanning electron microscopy images of fabricated square lattices (a_1 = 450 nm and a_2 = 350 nm) of Al NPs, and schemes of three different dyes incorporated with the two lattices. (b) Measured transmission spectra of the two lattices, and red, green, and blue lasing spectra. Transmission spectra of a_2 = 350 nm lattice were shifted down 0.3 for clarity. Lasing spectra of C500 and DCM are shifted up for clarity. (c) CIE plot of lasing emission profiles. BR1, BR2, and BR3 refer to the lasing spectra in Fig. 2b with dye mixing ratios 10 : 2, 10 : 2.5, and 10 : 3. BG1, BG2, and BG3 refer to the lasing spectra in Fig. 4b from bottom to top, and GR1, GR2, and GR3 refer to the lasing spectra in Fig. 4c from bottom to top. (d) Lasing emission spectra with a mixture of red, green, and blue dyes. (e) Photo of the far-field emission profile. The collection angle of the CCD detector is about 3°. Reproduced (or Adapted) with permission.[40] 2021, Wiley.

shown as yellow and cyan hues. The authors intended to offer a laser architecture that, thanks to the widely spaced RGB wavelengths and the small lasing linewidths, may enable a wide variety of accessible colors. The authors blended the DCM, C500, and C480 dyes with an ideal mixing volume of 3 : 2 : 10 to get a white-light lasing profile (Fig. 15d and corresponding CIE XYZ point in Fig. 15c). To provide the optical gain for the blue lasing, a higher volume of C480 solution was employed since the emission of C480 dye overlaps with the absorption of C500 and DCM dyes. The image in Fig. 15e depicts lasing in white color at the beam's focal point.

Numerous nanoparticles play a function in the creation of the WL, as has been demonstrated thus far in ref. 40 and 42. The subsequent work presents the merging of the Titanium Dioxide (TiO_2) nanoparticles' properties with the three organic dyes (CM440 – blue emission, CM6 – green emission, and Oxazine – red emission). The role of the used NPs is to induce scattering and provide intensity feedback while the organic dyes are responsible for the gain. Fig. 16a demonstrates the four photographs present the color tuning obtained by pumping at a wavelength of 355 nm. Blue and green color monochromatic emissions are pumped by the 355 nm, while the red one is excited with the 532 nm. The pump beam initially excites CM440 and CM6, and a portion of the CM6 peak pumps Oxazine. The white emission can be noticed when the three colors are combined.

The system may be created by combining a variety of different laser dyes. The results from employing CM440, CM153, and Oxazine are shown in Fig. 16b. When pumped with a 355 nm pulsed laser beam, the central wavelengths of the excited spectra of CM440 and CM153 are 431.8 nm and 541.65 nm, respectively, with linewidths of 6.06 nm and 10.4 nm, while the central wavelength of the exciting spectrum of oxazine is 647.42 nm with a linewidth of 4.8 nm when pumped by a 532 nm.

Fig. 16c shows the white light emission spectrum. The three peaks have linewidths of 9 nm, 32.24 nm, and 25 nm, respectively, and are located at 445.23 nm, 526 nm, and 644.5 nm. This outcome is significantly superior to the one where there

were no NPs. The spectra linewidths are shortened while the lasing thresholds are decreased with the application of TiO_2. Another crucial parameter is the NPs concentration; if it is too low, sufficient feedback won't be provided. If the concentration is too high, there are expected significant energy losses. The authors report that after experimenting with several concentrations, 0.025 mg mL^{-1} of TiO_2 was found to be the best concentration.

Another work demonstrates the hybrid Photonic Bandgap (PBG) White Laser.[145] The device consists of two similar inorganic multilayer photonic crystals sandwiching a soft photonic crystal (PC) or a layer of dye-doped cholesteric liquid crystal (CLC). A mono-, bi-, or tri-chromatic laser may be created using just one source of the optical pump. The hybrid has electrically tunable laser wavelength thanks to the soft PC that is controlled by the applied voltage. Dual-mode lasing, also known as simultaneous band-edge- and defect-mode lasing, exists in this artificial mixture of laser gain materials. Two of the emissions are on the Bragg Reflection (BR) band's edges, while the other comes from the defect mode's spiky transmission in the spectral PBG. This study's "coupled" PC (CPC) is a consolidation of a dye-doped CLC (DDCLC) sandwiched by two unusual dielectric mirrors acting as imperfect, one-dimensional (1-D) PCs. Contrary to single-mode lasing, the BR band of the organic PC and the PBG of the two identical inorganic PCs are said to be "connected" but assigned to distinct spectral areas.

Fig. 17a displays an actual image of the CPC as a laser device together with the CIE1931 color space chromaticity diagram identifying the color emitted by the discrete WL. The emission spectrum shown in Fig. 17c was used as the basis for calculating the color space data. The primordial color mixing of the three STE spectra is represented by the Y point, which has coordinates of $(x, y) = (0.3831, 0.5308)$. The W point ($x = 0.2459$; $y = 0.3637$), on the other hand, collects the additional dispersed intensity of the pumping light (*i.e.*, mixing of four colors at wavelengths of 446, 507, 550, and 632 nm). The lasing intensity of CPC is shown in Fig. 17b as a function of pumping energy. Around 7.4 mJ per pulse, a threshold beyond which the emission intensity sharply increased is noticed. The somewhat higher threshold in this case results from the additional energy needed to push the blue component into laser action. It should be noted that the lasing threshold was determined from the experimental setup, where the DDCLC cells were excited using an Nd:YAG pulsed laser. A half-wave plate and a linear polarizer were used in combination to regulate the incident pulsed energy, adjusting the pumping energy of the incident pulses. Fig. 17c shows the transmittance spectrum of the CLC alone as well as the emission and transmittance spectra of the CPC in the planar form. It is evident that the defect-mode lasing intensity was substantially larger than the fluorescence intensities associated with the BR

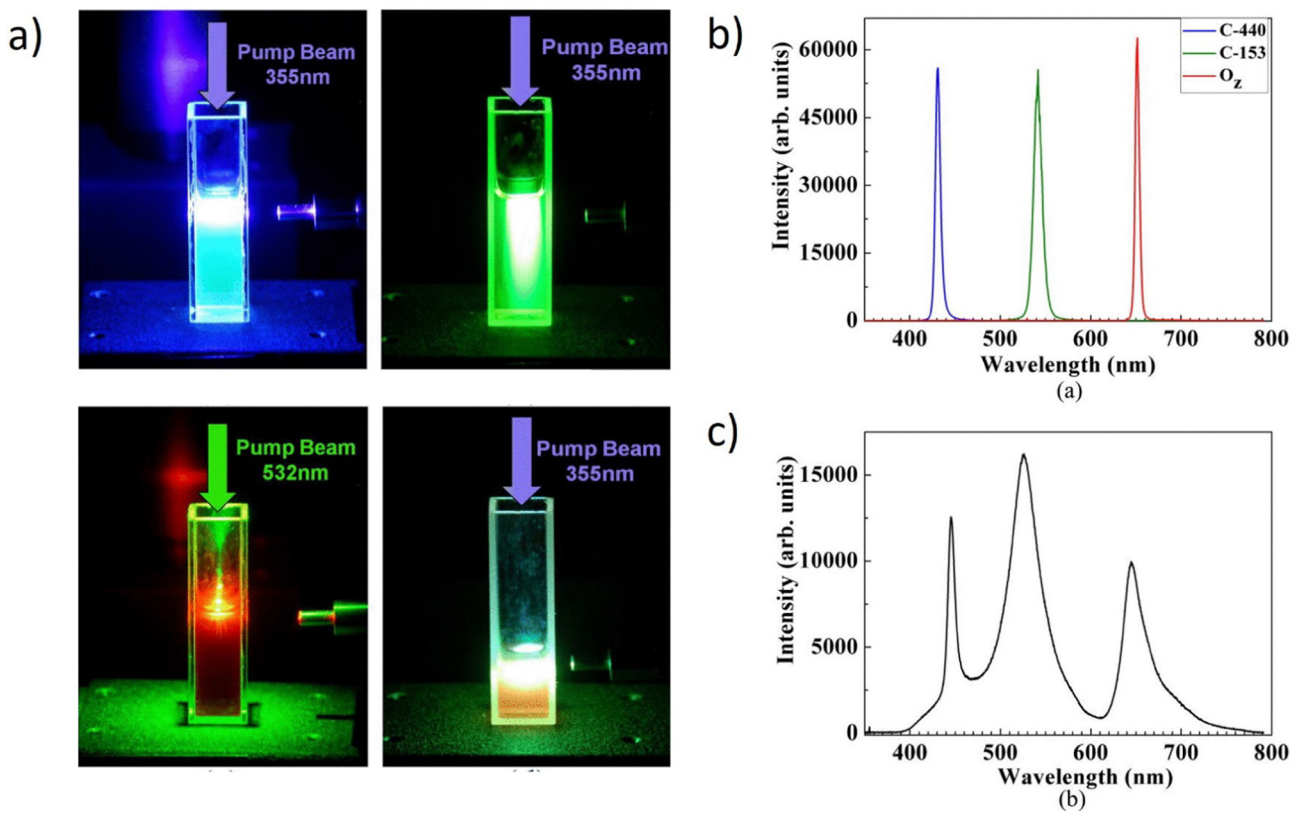

Fig. 16 (a) Photographs of the working of the system. Dyes emission of the mixed solutions when pumped by a single 355 or 532 nm pulsed beam. (b) Experimental results using CM440, CM153, and Oz laser dyes. (a) Excited spectra of CM440, CM153, and Oz. The CM440 and CM153 are pumped with a 355 nm pulsed laser beam, and the Oz is pumped with a 532 nm laser beam. (c) The spectrum of white light emission. The three peaks are at 445.23 nm, 526 nm, and 644.5 nm, and their linewidths are 9 nm, 32.24 nm, and 25 nm, respectively. Reproduced (or Adapted) with permission.[41] 2012, American Institute of Physics.

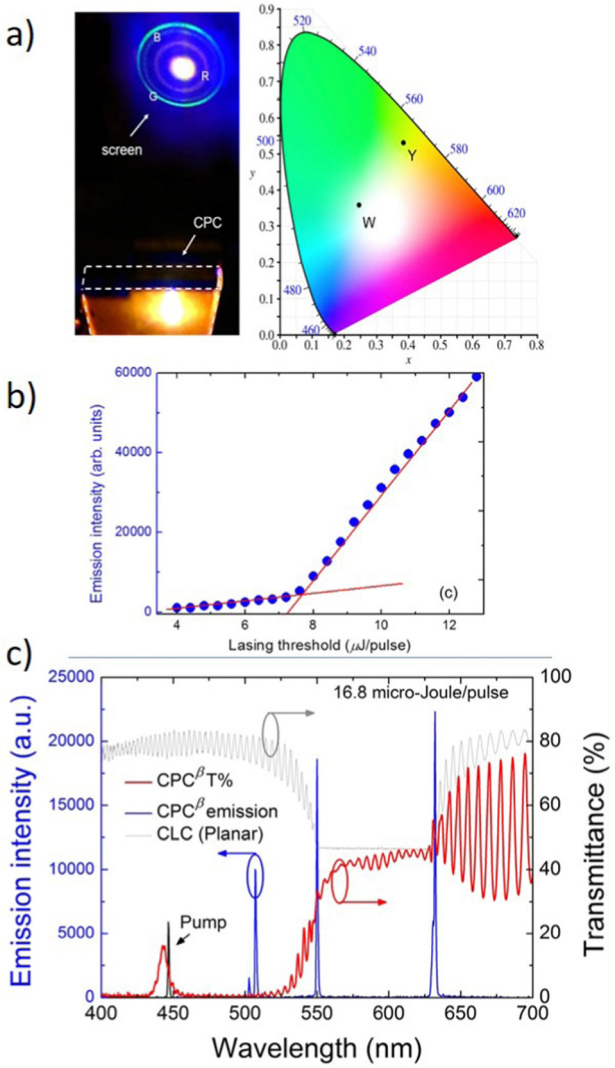

Fig. 17 (a) Photograph of a tricolor CPC laser device and its discrete emissions on a screen and the true color space coordinates of the laser on the CIE 1931 chromaticity diagram. (b) the pumping energy-dependent intensity of the lasing emitted from the CPC$^{\beta}$ device. (c) The white-light lasing spectrum and the referencing transmittance spectra of CPC$^{\beta}$ and the CLC alone in the planar state. Reproduced under terms of the CC-BY license.[145] 2016, Springer Nature.

band-edges, most likely as a result of the dyes reabsorbing some of the blue emission. The difference between the two at the BR's edges is explained by the cavity's standing waves' preferred polarization, which favors the long-wavelength side. The defect-mode laser in this example contributes to the shorter-wavelength hue (bluish-green) while the other two, (found at 632 nm and 550 nm), respectively, emit in red and green. The dye's ability to absorb pumping light of a shorter wavelength to allow greater absorption at the chosen emission means that the preferred blue emission, at 450 nm, from CPC is assigned to the dye's absorption and illumination spectra. A satellite peak (at 502 nm) on the left shoulder of the "blue" peak, which may be seen by carefully examining the emission spectra, may indicate that the control of the single defect-mode emission was less effective than in CPC.

The finding of room-temperature white-light amplified spontaneous emission (ASE) by carbon nanodots (C-dots) was described by Zhand *et al.*[99] The high-power laser serves as a source and the optical gain per peak power of the C-dots scattered inside *N*-Methylpyrrolidone (NMP) was found to be 64 cm^{-1} MW^{-1} at the peak wavelength.[146] The picture of the C-dots captured by TEM (Transmission Electron Microscopy) is depicted in Fig. 18a.

A small amount of the C-dot and NMP combination is deposited onto a TEM grid. According to the TEM picture, the size of the C-dot varies roughly between 1.5 and 3.5 nm. The mixture is added to a UV quartz micro-cell where the C-PL dot's properties are measured. A picture of a micro-cell with a mixture of C-dot and NMP is shown in Fig. 18b. The mixture has a consistent light-brown tone, which suggests that the C-dots ought to be spread evenly throughout the volume. These photos show C-dots scattered inside NMP while being excited using a quadruplet Q-switched Nd:YAG laser operating at 266 nm in pulsed operation (6 ns, 10 Hz) which leads to the ASE emission of extremely intense white light. Fig. 18c and d depict the so-called light in-light out curve and the emission spectra of the mixture as determined under 266 nm laser excitation at room temperature. The mixture's emission is captured during analysis from the shorter side of the micro-cell, which has an internal width of 2 mm and faces perpendicular to the laser beam's direction. It should be noted that the characteristic "kink" at an input intensity of around 0.21 MW cm^{-2} represents the change of the radiative process from SE to ASE. Furthermore, the full-width at half-maximum (FWHM) parameter *versus* peak intensity shows that the linewidth is narrowing nearly at the same point as the characteristic inflection is noticed.

For the interesting organo–inorganic devices emitting White Light on the way of lasing, it is worth mentioning that the

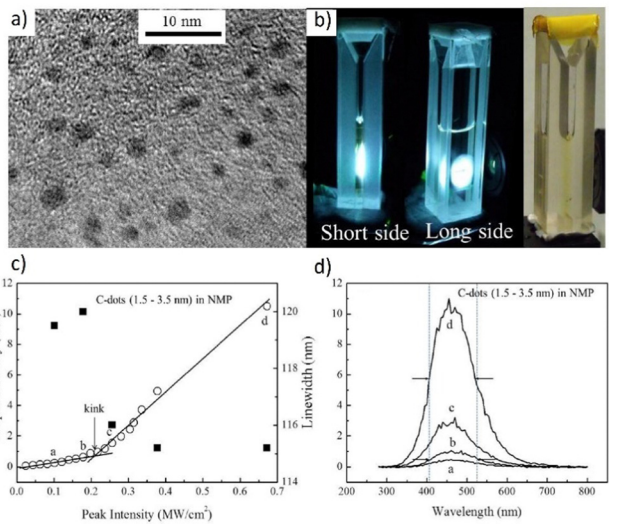

Fig. 18 (a) TEM images of C-dots, and (b) Photos of C-dots dispersed inside NMP. (c) Plot of PL intensity as a function of excitation light intensity, and (d) FWHM of the emission spectra of the C-dots and NMP mixture under 266 nm laser excitation at room temperature. Reproduced (or Adapted) with permission.[146] 2012, OSA Publishing.

hybrid multichannel metal-cladding slab-capillary microcavity discussed in ref. 71.

The authors have demonstrated that in the resonance cavity with its dimensionality much larger than the wavelength scale, the pump threshold can be significantly lowered. The use of an asymmetrical metal-cladding waveguide (SMCW) construction was crucial to obtain this result. Fig. 19a and b present the slab-capillary mode cross-coupled microcavity with a thickness ranging from 30 to 50 nm (for the metal substrate, the thickness is about 300 nm). The radius of the internal capillary is characterized by a radius of 0.1 mm and a glass slab with a thickness of 0.1 mm.

The SMCW function is to improve the resonance modes' excitation in the gain medium. This waveguide chip features an active medium-filled resonant cavity that is millimeters thick. This construction supports thousands of guided modes, that is, ultrahigh order modes (UOMs).[147] The authors stimulated the UOMs in the chips with and without capillaries. The UOMs for the chip are connected inside the capillary. The spectral reflectance in the slab (slab-capillary) waveguide, R1 (R2), is measured experimentally as a function of incidence angle in the 0°–5° range. The standing optical field quickly oscillates across the linear cavity between the metallic coupling layer and substrate at small incidence angles. Strong field amplification, excellent sensitivity, and polarization independence are only a few of the intriguing results.[148] The authors decided to improve the structure to eliminate background noise. The multiple capillaries were integrated into the slab, which forms a multichannel hybrid

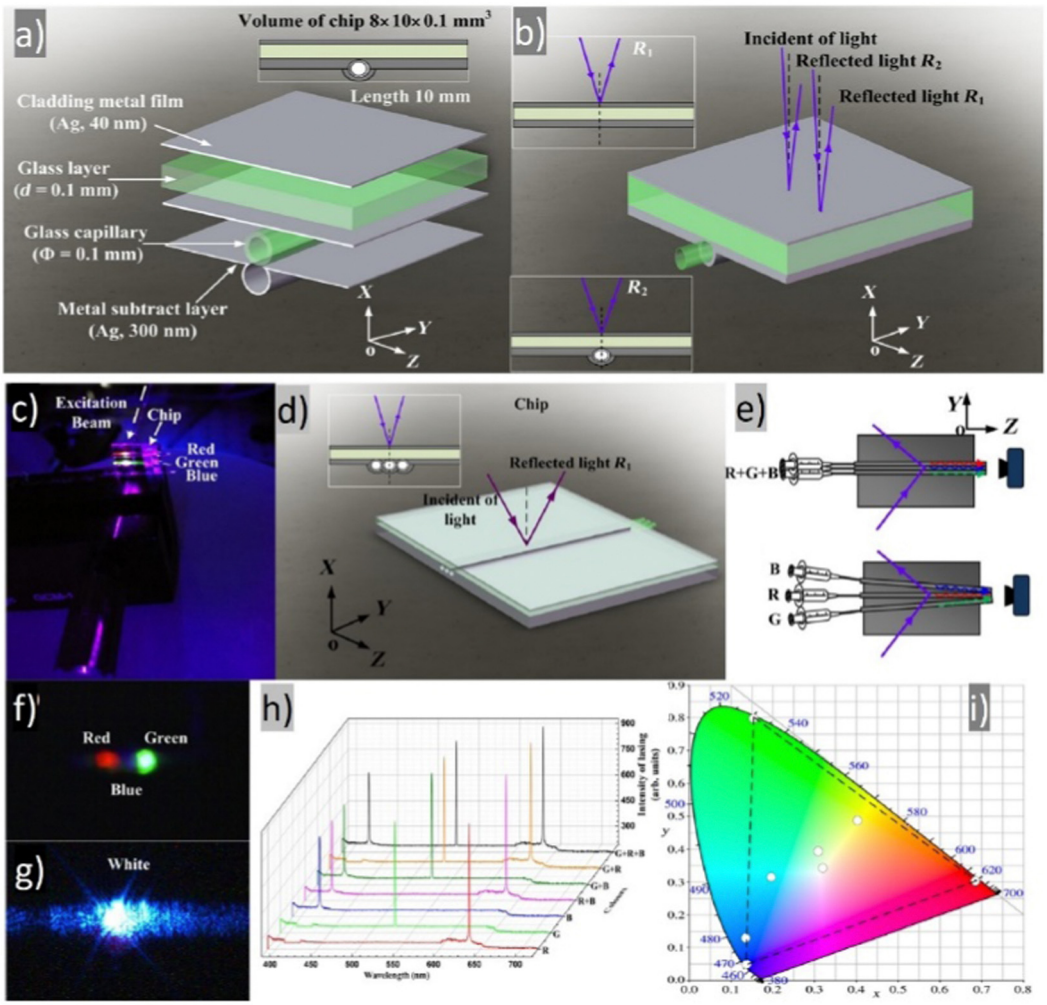

Fig. 19 Structure of the slab-capillary mode-cross-coupled microcavity. (a) Schematic diagram of the hybrid microcavity. (b) Excitation of the UOMs *via* free space coupling technique in slab waveguide (reflectance R1) and slab-capillary waveguide (reflectance R2). RGB and white lasing: (c)–(e) The pump beam illuminates the upper surface of the triple hybrid microcavity chip. The three capillaries are placed side by side. SB420, CM540, and R610 dye solutions are injected into the capillaries. The bottom picture presents adjusting the inclination of the capillaries, the RGB lasing beam converges to a point to form a white lasing point. (f) The image shows the RGB lasing points excited side by side in the chip structure. (g) White lasing point. (h) Lasing spectra when the blue (B), green (G), red (R), red and green (R + G), green and blue (G + B), red and blue (R + B), and red, green and blue (R + G + B) segments are pumped above their respective thresholds. (h) The chromaticity of the lasing peaks is shown as seven white circles extracted from the spectra in (i). The chromaticity of the R + G + B lasing is close to the CIE standard white illuminant D65. Dashed lines indicate the range of the achievable color palate for this particular chip. Reproduced (or Adapted) with permission.[71] 2019, APS.

microcavity with low background noise to support multicolor lasing. Fig. 19c–e demonstrates the experiment of the multicolor lasing. The three primary colors—stilbene 420 (SB420), CM 540 (CM540), and rhodamine 610 (R-610) are represented by the organic dyes and for the experiment were dissolved in the ethanol. The single capillary waveguide chip's cavity is filled with a dye solution using a syringe pump to produce a single wavelength lasing. All three capillaries are simultaneously illuminated by the 1 mm-diameter pumping area. The corresponding capillaries are injected with the dye solutions SB420, CM540, and R-610 (Fig. 19f and g). The authors show one-color lasing of each RGB color, simultaneous two-color lasing of any two of the three primary colors, and finally simultaneous RGB lasing of all three by pumping above the lasing threshold. The emission spectra for each of the seven combinations are shown in Fig. 19h. Red, green, blue, yellow, cyan, magenta, and white colors are demonstrated in the CIE color chart (Fig. 19i), respectively. Additionally, Grassmann's law states that any color inside the triangle pattern created by the three primary colors may be created by properly combining the three colors. The precisely calibrated white lasing's chromaticity is extremely similar to the white point of the CIE standard white illuminant.[149]

3.3. Organic

The interest in fully organic White Lasers is mainly motivated by their low cost, flexibility, environmental friendliness, excellent tunability, great compatibility, easy integration, and facile materials modification by either chemical synthesis/functionalization or by blending different fluorescent molecules.[150–153] White and multicolor lasers based on organic materials have a great future, at least according to the fact that they are now widely used in industry, *e.g.* as OLED displays.[154,155] In this respect, for the color depth and saturation, they are currently pioneering. The main limitation of organic materials is their photostability, which has to be constantly improved. Therefore, researchers have to face this difficulty, which makes the WRL still a challenging but extremely appealing topic.

Intriguingly, scores of scientific publications point out the potential of liquid crystalline micro-resonators for many applications in photonics and optoelectronic purposes.[99,156–159] The organic White Lasing (oWL), obtained with the help of the very appealing LC matter is reported in Light: science and Application.[38] The whole device relies on the phase separation of the investigated organic materials. The method uses three fundamental optically active materials that can be combined in different ways: pure PVA (poly(vinyl alcohol)) with hydrophobic LC droplets containing green-emitting CM540, pure PVA with hydrophobic LC droplets containing red-emitting DCM dye, and PVA hydrophilic matrix doped with blue-emitting organic dye- SB420. The absorption and emission spectra are presented in Fig. 20a.

The creation of this system was built layer-by-layer by the spin-coating system to separate all the colors and avoid energy transfer between red, green, and blue-emitting dyes. The macro-photograph presenting the device can be found in Fig. 20b. In PVA, the droplet size spans from 10 to 300 m, and the average distance between neighboring droplets is about 170 mm. The different microdroplet colors are demonstrated in Fig. 20c and the cross-polarizer mode, detecting the birefringent LC resonators immersed in a dark background can be seen in Fig. 20d. The planar alignment of LC droplets is illustrated as a sign of nematic LC order. By implementing this approach, it was possible to achieve well color- a separated system (confocal picture, Fig. 20e) resulting in three-color beams coming from the prepared sample (Fig. 20f) with the clearly defined lasing threshold (Fig. 20g), indicating the pumping fluence. The CIE XYZ chromaticity triangle demonstrates the color-tunability and the WRL point. The emission spectra are estimated using the CIE coordinates at an excitation fluence of 15 mJ cm^{-2}, which is over the lasing threshold. This illustrates the capability of precisely calibrating the emission color and generating white light that is balanced (CIE coordinates of 0.31, 0.32, and 0.37). Changing the excitation strength only a little bit will allow you to fine-tune the white emission from cool to warm tones. An oWL device with appropriate electrical contacts is depicted in Fig. 20h, where the active material is sandwiched between two transparent and conductive indium tin oxide (ITO) layers that have been formed on quartz substrates. The oWL emission intensity is guided in this way, varying up to about 80% of the maximum value for applied voltages up to 10 V. (Fig. 20i). This makes it possible to easily adjust the output of the oWL by turning on and off the applied field (inset of Fig. 20i). The tunability was possible to achieve since the LC matter has the unique property of changing the molecular alignment by application of external fields (in this case – electric field). In Fig. 20i, one can notice that the intensity of emitted white light can be easily modulated by the application of only 5 V. Moreover, the whole process is fully reversible, since LC molecules restore the position after the voltage is off. In contrast, the spectral emission characteristics of oWLs are unaffected by the electric field, with the CIE coordinates essentially remaining the same after numerous turns of the electric field on and off.

The next, fully organic system presents the two types of multicolor RGB laser-produced on the mechanically-flexible glass.[37] The first system is a multicolor laser array built by three individual lasers, emitting in red, blue, and green color, juxtaposed onto the substrate which is a flexible glass (Fig. 21a). Herein, the transparent polymer plays the role of encapsulation. The blue laser is the first to absorb the pump, followed by the green and lastly the red lasers. The goal of this arrangement is to minimize the discrepancies in the optical densities and oscillation thresholds of the BBEHP-PPV (-conjugated poly[2,5-bis(2′,5′-bis(2″-ethylhexyloxy)phenyl)-*p*-phenylene vinylene]), T3 (a star-shaped tris(terfluorenyl), and linear-c DPP lasers.

The second device is a stack of three independent RGB lasers placed on the same substrate (Fig. 21b). The three R, G, and B lasers mentioned above are layered on top of each other to create the second laser format. The individual monochromatic layers are separated by PVA and epoxy coatings. Therefore, the vertical separation between the DFB cavities is greater than 43 mm, preventing any unfavorable mode coupling. As a result, the DFB lasers oscillate independently, allowing the system as a whole to operate steadily over many wavelengths. According to Fig. 21b, the placement of the DFB lasers results in the pump being

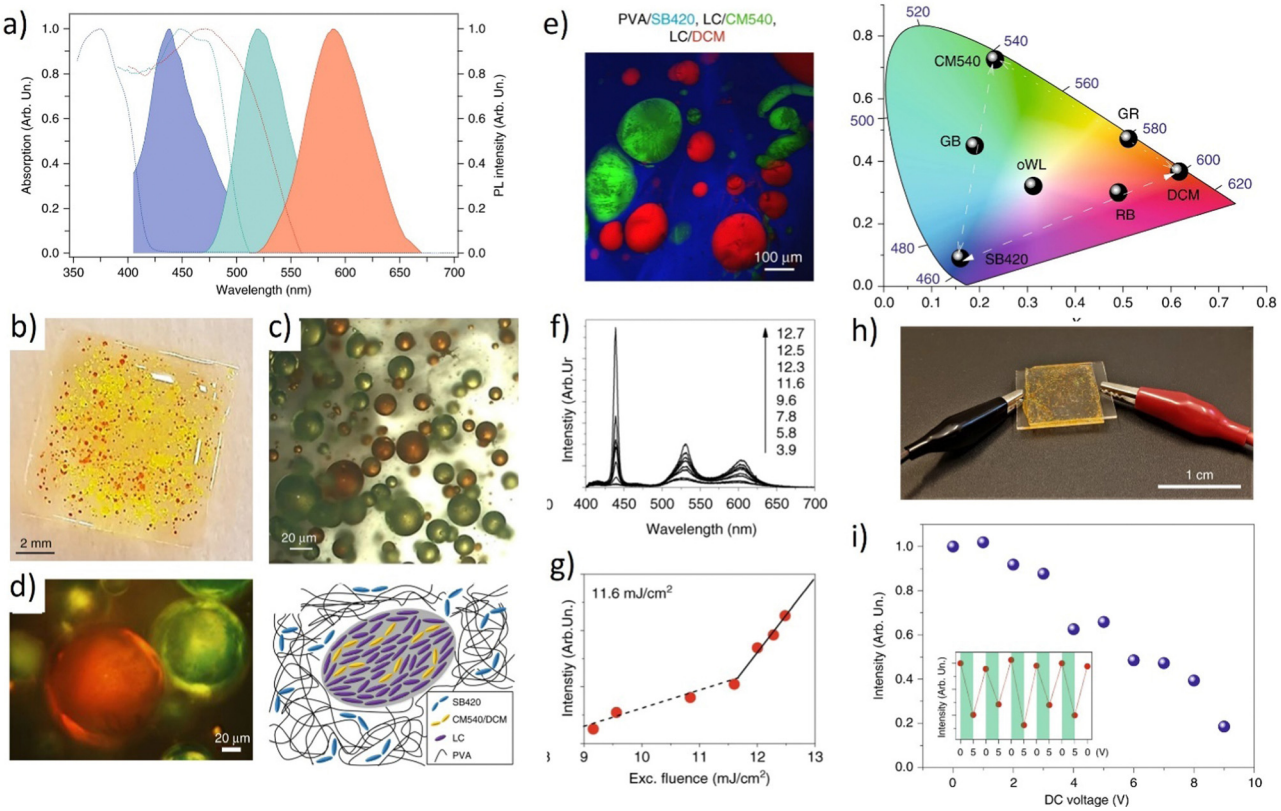

Fig. 20 (a) Absorption and photoluminescence spectra of the three elementary light-emitting materials. Blue lines: PVA/SB420; green lines: PVA + LC/CM540; red lines: PVA + LC/DCM; (b) sample photograph: SB420 and LC droplets are embedded in the PVA matrix. CM540 and DCM molecules are incorporated into the LC droplets; (c) corresponding optical bright field micrograph and the graphical representation of a cross-section of a region surrounding a single LC droplet in the multiphase system.; (d) crossed polarizer optical microscope picture (e) confocal fluorescence micrographs of samples containing PVA with SB420, LC/CM540, and LC/DCM together with CIE chromaticity diagram; (f). Corresponding lasing spectrum and (g) plot of the WLE emitted intensity *vs.* the excitation fluence; (h) photograph of an oWL device whose emission intensity is controlled by an externally applied voltage; (i) oWL emission intensity *vs.* applied DC voltage. The device is pumped at an excitation fluence of 11.9 mJ cm^{-2}. Inset: Lasing intensity for consecutive voltage cycles of 0–5 V applied to the device. Reproduced under terms of the CC-BY license.[38,72] 2020, Springer Nature.

absorbed first by the blue, then by the green, and finally by the red lasing layer. To minimize the differences in optical density and oscillation thresholds between the T3, BBEHP-PPV, and linear-c DPP lasers, this sequence was made (the red laser: 1,4-diketo-2,3,5,6-tetraphenyl-pyrrolo[3,4-*c*]pyrrole). In Fig. 21c, there are presented the white laser spectra obtained by the process of DFB lasing, together with the individual thresholds (Fig. 21d), pump energy fluence, and the photograph presenting the RGB "line" (Fig. 21e).

Fig. 22a demonstrates a strategy towards the development of a full-color WGM laser with the use of nested microcavity by partitioning three types of light-emitting polymers.

The light-emitting polymers PFO, F8BT, and MDMO-PPV were selected as the RGB components. Individual spectra of WGM lasing emission grow with the range of the pumping fluences from 17.7 mJ cm^{-2} to 74.2 mJ cm^{-2}, 25.3 mJ cm^{-2} to 71.6 mJ cm^{-2}, and 30.2 mJ cm^{-2} to 75.1 mJ cm^{-2}, respectively. Fig. 22b shows the expanded spectra. A spectroscopic ellipsometer is used to determine and fit the refractive index of the polymer solution. The FSR values of the microcavity are 0.1683 nm, 0.1662 nm, and 0.1634 nm at three distinct places labeled 1, 2, and 3 in Fig. 22a, respectively. One of the most crucial characteristics of the laser action are the designated lasing thresholds which are presented in Fig. 22c. It displays the output intensity for the WGM lasing and the full width at half maximum (FWHM) as functions of the pump energy density. The thresholds for the blue, green, and red emissions are 32.1 mJ cm^{-2}, 34.7 mJ cm^{-2}, and 33.2 mJ cm^{-2}, respectively, and can be noted as low in comparison with the other organic materials-based systems. What's more, there can be noticed similar values of designated thresholds, which can confirm the achievement of repeatable WGM cavity for RGB components, as well as the comparable emission efficiencies of gain materials. The calculations performed in the experiments use the formula of $Q = \lambda/\Delta\lambda$, in which λ is 550 nm and $\Delta\lambda$ is 0.025 nm and the Q factor reaches the level of 10^4 and the linear relationship between the Q factor and the capillary diameter is also validated. Fig. 22d demonstrates the photographs of the RGB mixtures in the full-color WGM laser. The various polymers in the nested microcavities can be easily changed for the wavelength-tunable microlasing. The maximum wavelengths of lasing for three PFO, F8BT, and MDMO-PPV polymer solutions are 455 nm, 545 nm, and 595 nm, respectively. When each of them is pumped above the thresholds, the two-colored (G + B), (R + B), and (R + G) PL pictures can be produced.

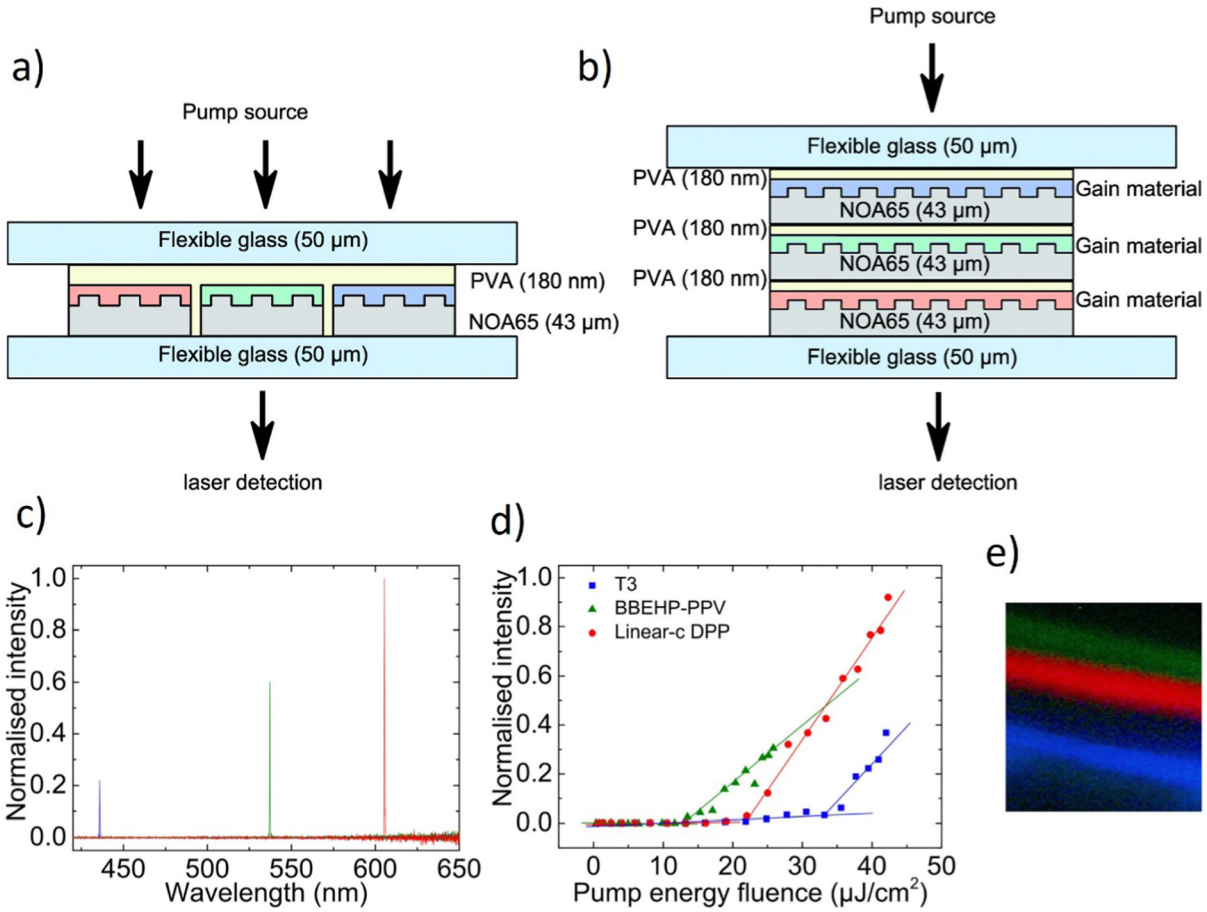

Fig. 21 Structure of the two RGB devices with (a) the "line" design and (b) the "stack" design. The arrows indicate the incident pump and the RGB laser output. (c) Spectrum, (d) pump energy fluence, and (e) photograph of the "line" RGB. Reproduced (or Adapted) with permission.[37] 2016, OSA publishing.

Moreover, the RGB lasing could be gathered and presented in the top graph of Fig. 20d when three polymers are supplied into the nested microcavity. The chromaticity diagram is depicted in Fig. 22e and features seven circles that represent various RGB component combinations. The color spectrum is covered by the connecting lines for the seven circles. The combined white light's CIE value is indicated by the "R + G + B" circle. The authors have presented a simple and effective strategy to obtain white laser taking advantage of the WGM lasing phenomenon in the compact device.

The next interesting publication refers to the white non-resonant ASE phenomenon. The general physical basis between the ASE and lasing is that when an optical resonator is present, an ASE can give rise to the lasing process,[160] and ASE itself can be described as amplification without feedback. For the ASE, there can be defined some characteristics, like the emission threshold, full width at half maximum (FWHM), and center emission wavelength. The ASE process can be recognized as the indicator, showing if the particular materials may be investigated as optically active medium or not. The fluorescent dye 4-(dicy-anomethylene)-2-*t*-butyl-6(1,1,7,7-tetramethyljulolidyl9-enyl)-4*H*-pyran (DCJTB) doped semiconducting poly(9,9-dioctylfluorene) (PFO) polymer thin films are optically pumped to produce the white ASE. The two emissive peaks are shown in Fig. 23a, including an ASE at around 440 nm that results from a structured blue band of PFO and was achieved on the DCJTB:PFO film with a 0.3% dye doping concentration.

The ASE at 605 nm from DCJTB appears when the pumping energy is raised to 0.07 mJ pulse^{-1}. Fig. 23b shows the peak, visible at 530 nm, which is ascribed to the PFO's g-band emission, whereas peak b is the consequence of ASE from DCJTB. The authors decided to examine the influence of dopants concentration. The ASE characteristics of the DCJTB:PFO thin film are shown in Fig. 23c to be substantially dependent on the DCJTB doping concentration in PFO. An ASE from PFO and a broad spontaneous emission from DCJTB are seen at a low doping concentration of 0.1%, showing that the energy transfer from PFO to DCJTB is minimal in this case. The average host–guest separation distance reduces and the energy transfer rises when the doping concentration is increased to 0.3%. As a result, ASE spectra are acquired from both PFO and DCJTB. Higher doping concentrations (0.5%) result in a full transfer of exciton energy from PFO to DCJTB, which leaves just DCJTB as the active substance. It is evident that DCJTB:PFO produces the best White ASE white at 0.3% doping concentration with a trichromatic coordination value of (0.42, 0.35). For PFO and DCJTB, independently, there was also designated the ASE energy threshold at 0.035 and

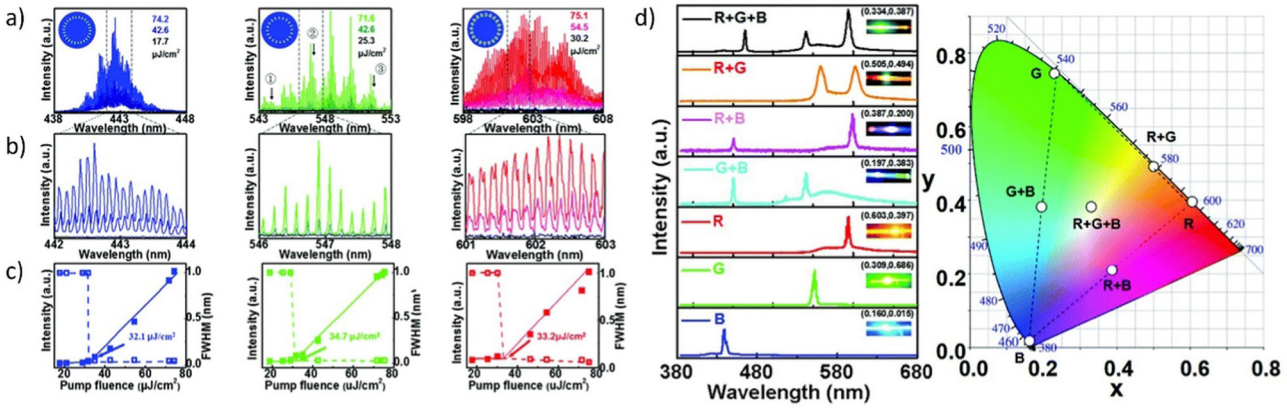

Fig. 22 (a) The spectra of RGB lasing with excitation on the blue-emission, green-emission, and red-emission; the top left illustration shows the distribution of electric field intensity in the transverse cross-section respectively. are denoted as ①, ②, and ③, respectively. (b) Enlarged PL emission spectrum for blue, green, and red-emission, respectively. (c) The intensity and FWHM of the output at different power densities. (d) PL images corresponding to the laser spectrum with various nested microcavity devices of RGB pumped above the thresholds. The top right illustration shows the PL of RGB and the numbers show the CIE1931 coordinates calculated from the corresponding spectra. From bottom to top: blue (B), green (G), red (R), green-blue (G + B), red-blue (R + B), red-green (R + G), and red-green-blue (R + G + B) emission and chromaticity of the laser central wavelength extracted from the spectrum in (a) with seven white circles. The black dashed lines demonstrate the range of RGB emission. Reproduced (or Adapted) with permission.[33] 2021, RSC Publishing.

0.072 mJ pulse^{-1} (Fig. 23d). Such a result is interesting and indicates the possibility of obtaining a white laser using a similar system in the future.

For the full-color laser displays with a distinguishing color gamut, it is important to mention organic printed microlaser arrays, published in Nature Communications.[162] Fig. 24a demonstrates the design and fabrication of the system. Several methods are used to selectively print organic ink solution droplets at precise spots on surfaces to build organic microlaser arrays. The substrate is first treated with a thin coating of 1*H*,1*H*,2*H*,2*H*-perfluorooctyltriethoxysilane to provide a hydrophobic effect. This technique can significantly aid in the creation of each droplet's spherical cap shape. Capillary action is used to absorb ink solution through a glass needle, followed by ultrasonic vibration-assisted spraying of a drop onto the hydrophobic substrate. The ink droplets are spread in a spherical cap shape and harden when water evaporates, as seen in Fig. 24b. The microstructures are reproducible, uniform in size, and can be used as building blocks to create microcavity arrays with high packing density. Each microspherical cap serves as an excellent high-quality WGM cavity to support laser oscillations. To provide the gain in the microspheres, the incorporation of different luminescent dyes into the ink is required. This allows for tuning the lasing wavelength range. By sequentially printing red-, green-, and blue-emissive inks (namely Rhodamine B (RB), fluorescein disodium salt (uranin), and SB420), with precise alignment, pixelated RGB spherical cap arrays can be created over a large area in a uniform geometric shape, which is vital for practical displays. Each group of three adjacent spherical caps forms a single pixel. Under UV light, the pixels emit bright RGB fluorescence, indicating the feasibility of printed microspherical cap arrays as full-color self-emissive laser display panels.

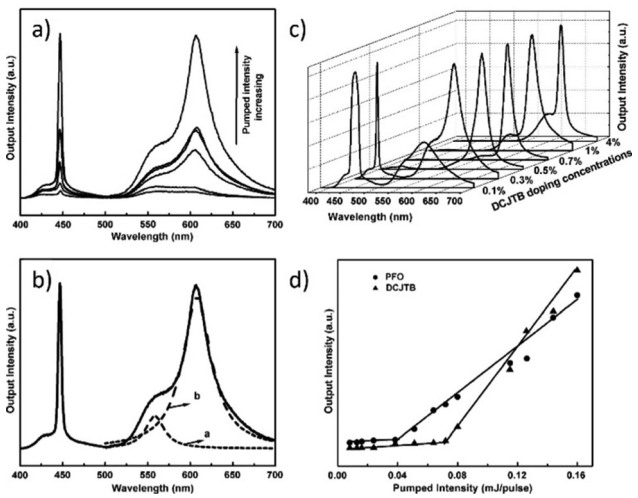

Fig. 23 (a) Normalized emission spectra of the DCJTB:PFO thin film (DCJTB doped concentration is 0.3%) at different pumped intensities. (b) The broadband emission from 530 to 680 nm consists of two peaks. (c) ASE spectra of DCJTB:PFO thin film with different doping concentrations of DCJTB at the pumped intensity of 0.12 mJ pulse mJ pulse^{-1}. (d) Output emission intensity of the DCJTB:PFO film at the peak wavelength of 446 and 605 nm as a function of the pumped intensity. Reproduced (or Adapted) with permission,[161] 2008, American Institute of Physics.

Fig. 24c represents the multicolor tuning which was realized *via* the analysis of the emission spectra coming from a single pixel to assess the emitted color. By excitation of different color pixels, it was possible to tune between the whole color gamut of lasing emission (starting from single colors RGB, then exciting the pairs: R-G, G-B, and R-B, and with the final achievement of RGB laser). To determine the chromaticity of the lasing spectra, a CIE1931 color diagram was used to plot the results (Fig. 24d). The emissions were observed in blue, green, red, cyan, magenta, yellow, and white accordingly. The balanced white lasing (B-G-R) was found to have a chromaticity close to that of the CIE standard white illuminant D6541.[162]

Real color images of pixelated laser arrays were obtained under laser irradiation to investigate the realistic color rendering in the far field. Similar to the last experiment, these hues were created by combining light emitted by spherical cap microlasers. By printing separate inks on an identical substrate, an ''ICCAS'' pattern of microlaser arrays was created. The far-field picture of the created patterns was taken using the built-in digital camera of a mobile phone, which was easily recorded by the naked eye (Fig. 24e). When the arrays were created simply using inks doped with S420, uranin, and RhB, the patterns displayed blue, green, and red hues, respectively. Furthermore, the mixed lasing emissions colors identified were cyan, magenta, and yellow. When pumping the RGB pixelated ''ICCAS'' pattern, the lasing

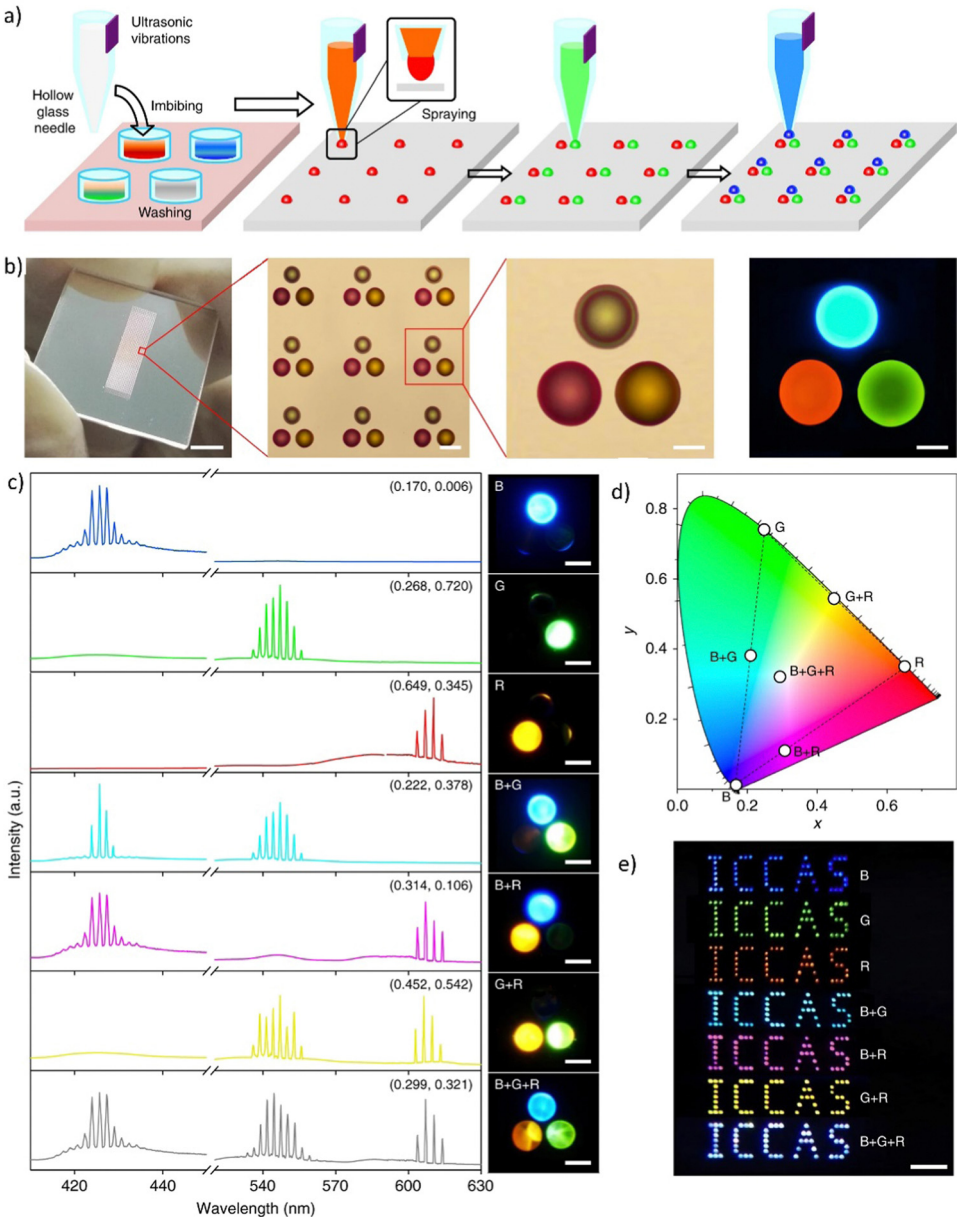

Fig. 24 (a) Schematic illustration of the fabrication of organic RGB microlaser pixel arrays by ultrasonic vibration-assisted inkjet printing; (b) image of large-area ordered optical structures (The scale bar is 5 mm), together with microscopy images of the printed RGB pixel array showing the uniform size and a well-defined pattern. The scale bars are 50 and 20 μm, respectively. The last picture on the right side shows the fluorescence microscopy image of the printed RGB pixel under UV light radiation (330–380 nm). The scale bar is 20 μm; (c) lasing spectra and corresponding photoluminescence images when different positions of the RGB pixel were pumped above their thresholds. From top to bottom: the blue (B), green (G), red (R), blue and green (B + G), blue and red (B + R), green and red (G + R), and blue, green and red (B + G + R) emissive spherical caps. The numbers show the CIE1931 coordinates calculated from the corresponding spectra. All scale bars are 20 μm; (d) chromaticity of the lasing peaks extracted from the spectra in a, shown as seven white circles. The dashed lines indicate the range of the achievable color gamut for the RGB pixel; (e) far-field photograph of the ''ICCAS'' patterns of pixel arrays comprising different RGB emissive spherical caps. Mixed far-field emission colors of blue, green, red, cyan, magenta, yellow, and white were observed from the panel under UV excitation. The scale bar is 2 mm. Adapted/Reproduced with permission.[162]

emissions from all three spherical caps were simultaneously mixed, producing a white color. The implementation of the multi-primary spatial-temporal color synthesis indicates that the printed pixelated RGB laser arrays are very appealing and promising candidates for use in full-color laser display panels.[162]

In essence, to provide the summary of all the 16 scientific publications centered around the achievement of a WL or White ASE, a comprehensive compilation of the paramount findings is assimilated in Table 2.

The articles in the table are arranged based on the classification of the system type starting from inorganic, going to hybrid, and ending on organic ones. The table features a concise overview of the techniques and materials employed in each system, alongside the chromaticity coordinates for WL/White ASE attained through these approaches. The primary purpose is to exhibit the diverse methodologies, materials, and an overview of the research presented, all contributing towards the attainment of WLE.

4. Applications and perspectives

Concerning the applications, perspectives, and future possibilities to use White Lasing, it is worth mentioning the Li-Fi technology. The Li-Fi wireless system is founded on the concept to provide networking and high-speed communications systems and is based on the idea of white light emission with an examination of LEDs as a medium. The upgrade based on the idea of the laser might increase that speed to around 100 Gb s^{-1}, which is an order of magnitude greater than the previous LED-bulb-based Li-Fi technology. The Li-Fi system's technology is now the subject of extensive research and testing.[163–167]

The idea to merge the lighting and the data delivery can be supported by the research made by the Sandia Laboratory.[25] Solid-state lighting is currently based mostly on the use of LED or OLED sources of light. The experimental set-up was created by Sandia researchers, who combined the light from four lasers using chromatic beam splitters, then sent the combined light through several ground-glass diffusers to avoid speckles before

Table 2 Table demonstrating the summary of the articles discussing white laser emission, concerning system, methods, materials and CIE XYZ coordinates for "white" point

Title and reference	System	Methods	Materials	WL coordinates (x, y)
A monolithic white laser[116]	Inorganic	Semiconductor lasing	ZnCdSSe nanosheets	N/A
A highly-efficient single segment white random laser[62]	Inorganic	Random lasing Upconversion	Multicolor NPs on top of Au/MoO_3 Hyperbolic meta materials (HMMs)	HMM1 (0.333, 0.334); HMM 2 (0.334, 0.354); HMM 3 (0.334, 0.342)
Demonstration of a white laser with V_2C MXene-based quantum dots[16]	Inorganic	Nonlinear Random scattering system	V_2C MXene-based QDs	(0.349, 0.334)
White-light whispering-gallery-mode lasing from lanthanide-doped upconversion $NaYF_4$ hexagonal microrods[32]	Inorganic	WGM lasing Upconversion	Multicolor $Yb^{3+}Er^{3+}Tm^{3+}$ tridoped hexagonal β-$NaYF_4$ microrod	(0.3440, 0.3573)
Observation of white-light amplified spontaneous emission from carbon nanodots under laser excitation[146]	Hybrid	White ASE	Carbon nanodots into *N*Methylpyrrolidone (NMP) organic solution	(0.363, 0.356)
White beam lasing from a hybrid microcavity with slab-capillary mode oupling[71]	Hybrid	Metal-cladded slab-capillary microcavity chip	Dyes: SB420, CM540, R610 in ethanol solutions	N/A
Electrically switchable organo-inorganic hybrid for a white-light laser source[145]	Hybrid	Photonic bandgap lasing	A soft photonic crystal, (CLC), inorganic photonic crystals	(0.2459, 0.3637)
Plasmonic nanoparticle lattice devices for white-light lasing[40]	Hybrid	Plasmonic nanolasing	NPs in inorganic lattices dyes: CM480, CM500, DCM	N/A
A white random laser[36]	Hybrid	RL with on-chip integration Plasmonic	Dyes: R6G, and DCJTB, SB420 NPs, MPF with Ag NPs	Not given ("approaching that of the CIE standard white illuminant D65")
Chromaticity-tunable white random lasing based on a microfluidic channel[42]	Hybrid	Plasmonic laser In the capillary microfluidic channel	Au–Ag nanowires, dyes: CM440, CM153, R6G, CM460, oxazine, CM6	N/A
White light emission with red-green-blue lasing action in a disordered system of nanoparticles[41]	Hybrid	Random lasing	Dyes: CM440, CM6, oxazine, TiO_2 NPs	N/A
Electrically controlled white laser emission through liquid crystal/polymer multiphases[38]	Organic	Random lasing	Dyes: SB420, CM540, DCM matrices: LC, PVA	(0.31, 0.32)
RGB and white-emitting organic lasers on flexible glass[37]	Organic	DFB lasing	Flexible glass AF32, PVA, red oligomer linear-c DPP, green BBEHP-PPV polymer, blue star-shaped tris(terfluorenyl)	(0.33, 0.27)
White light emission on amplified spontaneous emission with dye content controlled polymer system[161]	Organic	White ASE	Dye DCTJB and PFO polymer	(0.42, 0.35)
Full-color WGM lasing in nested microcavities[33]	Organic	WGM lasing	Emissive polymers: PFO, F8BT, MDMO-PPV	(0.334, 0.387)
Full-color laser displays based on organic printed microlaser arrays[162]	Organic	WGM lasing Laser arrays	Dyes: SB420, fluorescein, RB and ink	(0.299, 0.321)

illuminating the test objects. The LED and diode laser-produced white light illumination was tested by the forty volunteers. According to experimental results, the human eye is equally comfortable with white light produced by diode lasers and LEDs. Considering that lasers have several advantages over LEDs, this innovation may have a significant impact on future technology. Specifically, LED efficiency declines over 0.5 amps but diode laser efficiency rises as electrical current increases. The advantages of laser technology include also achievable broader color gamut, stronger contrast ratios, and more vibrant colors.

Currently, laser lights are an absolute innovation in automotive lighting. Laser diodes are characterized by their compact and small sizes. The beam of light resembles a point with a diameter of the order of micrometers which means that very small lenses can be used to focus the strong and effective light. Today the brightness of laser light is almost four times higher than that of LED sources. Laser diodes mounted in automotive lamps emit monochrome light with a wavelength of up to 450 nanometers, which the human eye perceives as blue/purple. Light in this color would unfortunately be inappropriate for use in automotive lighting. Therefore, white light preferably with a color temperature of approximately 5500 K is still intensely sought.

Due to their wide angular spread of output emission and speckle-free image, random lasing devices can be also promising devices for display applications. Surprisingly, the White-RL lasing characteristics (frequency, linewidth, intensity, and chromaticity) are free of observation angles, which is an exclusive advantage for the next generation of light sources, with applications ranging from optical communication to lighting, display, and medical sensing.[36,95,120,168] Producing compact, energy-efficient, high-performance light-emitting optoelectronic devices is the overriding goal these days and lasers meet all of these requirements.

It seems that two methods of obtaining WL will continue to be developed, which rely on a single material that simultaneously emits lights of different wavelengths covering the visible spectrum and the combination of two or more light emitters of different colors. Undoubtedly, a breakthrough concept would be to create electrically pumped organic white lasers (EPOWLs). Such sources of light, due to the variety of available materials, have the potential for broad color tuning, thus allowing the implementation of active-matrix flexible laser displays with a high contrast ratio, which holds great promise for smart devices and equipment. However, this requires further development of multi-obstacle engineering solutions, and deep insight into the relationship between molecule structures, as well as cavity configurations.[169,170]

Perhaps such materials will turn out to be thermally activated delayed fluorescence (TADF) emitters. TADFs, which are characterized by a reverse intersystem crossing (RISC) process from triplet to singlet excited states, afford a promising solution for handling triplet-related losses. Very recently, it was shown that self-assembled TADF microcrystals exhibit well-defined structures and strong cavity effects. Therefore, thermally activated lasing (TAL) was obtained in as-prepared microplates in which RISC processes played an important part in utilizing triplet excitons. The excellent material compatibility of selected matrices enabled to tune of the lasing output wavelength over the full visible spectrum by doping them with various TADF gain media. Under programmable excitation beam scanning, laser displays were realized using as-prepared pixelated trichromatic TADF microlaser arrays as display panels. These results not only provide a novel approach for harvesting triplet excitons for stimulated emission in TADF micro crystals but also offer innovation for the pursuit of EPOWLs.[171]

Based on the irreplaceable features of organics such as flexibility, chemical tunability, and biocompatibility, compared with their inorganic competitors, the organic laser will play a very important role in future applications including white lasing.

Metal halide perovskites are also very promising candidates as gain medium for a thin-film electrically-pumped laser including WL. This is owing to their excellent optoelectronic properties. Optically-pumped lasing has been routinely observed from perovskite-based active layers in different resonator structures, while continuous-wave lasing has been realized not also at room temperature. All of these results indicated that these inorganic materials are promising alternatives for optoelectronic applications too.[172,173]

5. Conclusions

The recent discovery of the first White Laser shows a non-questionable breakthrough in future photonics and optoelectronics. Growing evidence suggests that white laser sources will be pursued and optimized as the technology of the future. In this review, we focused our attention on the 16 scientific publications concerning white lasers/white ASE. It clearly indicates that this topic is decidedly novel. In turn, it appears particularly evident that most of these articles are announced at an extremely fast pace (from 2015) showing a remarkable interest to seek for white lasers in this decade. Five of the articles refer to fully organic systems and four concern inorganic materials. The hybrid organic-inorganic systems were presented in the discussion of seven published papers. From the viewpoint of the investigated materials and techniques, we discussed different strategies *via* realizing the white lasers. The issues of energy transfer and its role, up-conversion, multicolor tunability, matrices' role, and arrangement of the optical cavities were presented and discussed in many literature examples. We also highlighted the advanced applications of white lasers: the ones that currently exist and the others, which are extensively studied and developed. Further research is needed to gain a deeper understanding of how to produce simplified, highly efficient, and photostable multicolor and white laser sources.

Abbreviation

A	Acceptor
ASE	Amplified spontaneous emission (ASE)
BR	Bragg Reflection
CDs	Carbon dots
CIE	Commission internationale d'eclairage

CLC	Cholesteric liquid crystal
CMx	CoumarinX
CP	Circularly polarized
CPL	Circularly polarized light
CPC	''Coupled'' photonic crystal
CT	Charge transfer
CVD	Chemical vapor deposition
D	Donor
DDCLC	Dye-doped cholesteric liquid crystal
DFB	Distributed feedback
DgPC	dibenzo[*g*,*p*]chrysene
E	The FRET efficiency
ESIPT	Excited state intramolecular proton transfer
EPOWL	Electrically pumped organic white laser
ETU	Energy transfer upconversion
FRET	Förster resonance energy transfer
FWHM	Full-width at half-maximum
HMM	Hyperbolic meta-material
LCs	Liquid crystals
LCFM	Laser confocal fluorescence microscopy
LED	Light emitting diodes
Li-Fi	Light fidelity
LSP	Localized surface plasmons
$MAPbX_3$	Methyl ammonium lead halide perovskites
MPFs	Monochromatic polymer films
MQDs	Metal carbides quantum dots
MSHNs	Multi-segment heterostructure nanosheets
NIR	Near-infrared
NMP	*N*-Methyl pyrrolidone
NPs	Nanoparticles
OLED	Organic light emitting diodes
oWL	Organic white lasing
PBG	Photonic bandgap
PC	Photonic crystal
PDOS	Photonic density of states
PL	Photoluminescence
PLQY	Photoluminescence quantum yield
PS	polystyrene
PVA	poly(vinyl alcohol)
QDs	Quantum dots
QLED	Quantum dot light-emitting diode
RAHBs	Resonance-assisted hydrogen bonds
RX	RhodamineX
REI	Rare earth ions
RET	Resonance energy transfer
RGB	Red, green, blue
RISC	Reverse intersystem crossing
RL	Random lasing
SANE	Solvent-assisted nanoscale embossing
SB420	Stilbene 420
SLRs	Surface lattice resonances
SMCW	Asymmetrical metal-cladding waveguide
SSL	Solid-state lighting
STE	Stimulated emission
TADF	Thermally activated delayed fluorescence
TAL	Thermally activated lasing
TEM	Transmission electron microscopy
TiO_2	Titanium dioxide
UCE	Up-conversion emission
UCNP	Up-conversion nanoparticles
UOMs	Ultrahigh order modes
V2C	Vanadium carbide
WGM	Whispering gallery mode
WGW	Whispering gallery wave
WL	White lasers
WLE	White light emission
WRL	White random lasing

Conflicts of interest

There are no conflicts to declare.

References

1 S. Joseph, *Organic Light-Emitting Devices*, Springer, New York, 2004.
2 F. F. Xu, Y. J. Li, Y. Lv, H. Dong, X. Lin, K. Wang, J. Yao and Y. S. Zhao, *CCS Chem.*, 2020, **2**(6), 369–375.
3 L. S. Sapochak, *J. Am. Chem. Soc.*, 2001, **123**(27), 6744–6745.
4 B. W. D'Andrade and S. R. Forrest, *Adv. Mater.*, 2004, **16**, 1585–1595.
5 K. T. Kamtekar, A. P. Monkman and M. R. Bryce, *Adv. Mater.*, 2010, **22**, 572–582.
6 J. H. Wei, J. F. Liao, L. Zhou, J. Bin Luo, X. D. Wang and D. Bin Kuang, *Sci. Adv.*, 2021, **7**, 34.
7 N. Dalloz, V. D. Le, M. Hebert, B. Eles, M. A. Flores Figueroa, C. Hubert, H. Ma, N. Sharma, F. Vocanson, S. Ayala and N. Destouches, *Adv. Mater.*, 2022, **34**, 1–8.
8 S. Kolemen and E. U. Akkaya, *Coord. Chem. Rev.*, 2018, **354**, 121–134.
9 D. Wu, A. C. Sedgwick, T. Gunnlaugsson, E. U. Akkaya, J. Yoon and T. D. James, *Chem. Soc. Rev.*, 2017, **46**, 7105–7123.
10 G. Chen, X. Li and X. Feng, *Angew. Chem.*, 2022, **61**, e202209014.
11 C. Basu, S. Schlangen, M. Meinhardt-Wollweber and B. Roth, *J. Med. Imaging*, 2015, **2**, 044501.
12 R. Singh, *World J. Gastrointest. Endosc.*, 2009, **1**, 45–50.
13 Z. Zhou, J. Zhao, Y. Du, K. Wang, J. Liang, Y. Yan and Y. S. Zhao, *Angew. Chem.*, 2020, **59**(29), 11814–11818.
14 M. V. Kovalenko, L. Manna, A. Cabot, Z. Hens, D. V. Talapin, C. R. Kagan, V. I. Klimov, A. L. Rogach, P. Reiss, D. J. Milliron, P. Guyot-Sionnnest, G. Konstantatos, W. J. Parak, T. Hyeon, B. A. Korgel, C. B. Murray and W. Heiss, *ACS Nano*, 2015, **9**, 1012–1057.
15 D. V. Talapin, J. S. Lee, M. V. Kovalenko and E. V. Shevchenko, *Chem. Rev.*, 2010, **110**, 389–458.
16 D. Huang, Y. Xie, D. Lu, Z. Wang, J. Wang, H. Yu and H. Zhang, *Adv. Mater.*, 2019, **31**, 1901117.
17 Z. Yang, J. Z. Fan, A. H. Proppe, F. P. G. De Arquer, D. Rossouw, O. Voznyy, X. Lan, M. Liu, G. Walters, R. Quintero-Bermudez, B. Sun, S. Hoogland, G. A. Botton, S. O. Kelley and E. H. Sargent, *Nat. Commun.*, 2017, **8**, 1325.

18 J. Guan, L. K. Sagar, R. Li, D. Wang, G. Bappi, N. E. Watkins, M. R. Bourgeois, L. Levina, F. Fan, S. Hoogland, O. Voznyy, J. Martins De Pina, R. D. Schaller, G. C. Schatz, E. H. Sargent and T. W. Odom, *Nano Lett.*, 2020, **20**, 1468–1474.
19 Y. Huang, E. L. Hsiang, M. Y. Deng and S. T. Wu, *Light Sci. Appl.*, 2020, **9**, 1–16.
20 X. Da, Z. Han, Z. Yang, D. Zhang, R. Hong, C. Tao, H. Lin and Y. Huang, *Chem. Phys. Lett.*, 2022, **794**, 139497.
21 A. Kokka, T. Poikonen, P. Blattner, S. Jost, A. Ferrero, T. Pulli, M. Ngo, A. Thorseth, T. Gerloff, P. Dekker, F. Stuker, A. Klej, K. Ludwig, M. Schneider, T. Reiners and E. Ikonen, *Metrologia*, 2018, **55**, 526.
22 T. Komine and M. Nakagawa, *IEEE Trans. Consum. Electron.*, 2004, **50**, 100–107.
23 J. J. Wierer, J. Y. Tsao and D. S. Sizov, *Laser Photonics Rev.*, 2013, **7**, 963–993.
24 R. Haitz and J. Y. Tsao, *Phys. Status Solidi Appl. Mater. Sci.*, 2011, **208**, 17–29.
25 A. Neumann, J. J. Wierer, W. Davis, Y. Ohno, S. R. J. Brueck and J. Y. Tsao, *Opt. Express*, 2011, **19**, A982–A990.
26 A. Dubietis, G. Tamošauskas, R. Šuminas, V. Jukna and A. Couairon, *Lith. J. Phys.*, 2017, **57**, 113.
27 V. P. Kandidov, S. A. Shlenov and O. G. Kosareva, *Quantum Electron.*, 2009, **39**, 205.
28 A. Couairon and A. Mysyrowicz, *Phys. Rep.*, 2007, **441**, 47–189.
29 M. Sasi Chandra, S. Saleem, S. L. Harish, R. Baskar and P. C. Kishoreraja, *Int. J. Pharm. Technol.*, 2016, **8**, 466–471.
30 X. Bao, G. Yu, J. Dai and X. Zhu, *Wirel. Networks*, 2015, **21**, 1879–1889.
31 R. R. Sharma and A. Sanganal, *et al.*, *Int. Res. J. Eng. Technol.*, 2017, **4**, 150.
32 T. Wang, H. Yu, C. K. Siu, J. Qiu, X. Xu and S. F. Yu, *ACS Photonics*, 2017, **4**, 1539.
33 K. Ge, X. Shi, Z. Xu, C. Libin, D. Guo, S. Li and T. Zhai, *Nanoscale*, 2021, **13**, 10792.
34 Z. S. Pehlivan, M. Torabfam, H. Kurt, C. Ow-Yang, N. Hildebrandt and M. Yüce, *Microchim. Acta*, 2019, **186**, 1–22.
35 A. Adamow, A. Szukalski, A. Justyniarski, L. Sznitko and J. Mysliwiec, *J. Lumin.*, 2020, **220**, 116903.
36 S. W. Chang, W. C. Liao, Y. M. Liao, H. I. Lin, H. Y. Lin, W. J. Lin, S. Y. Lin, P. Perumal, G. Haider, C. T. Tai, K. C. Shen, C. H. Chang, Y. F. Huang, T. Y. Lin and Y. F. Chen, *Sci. Rep.*, 2018, **8**, 2720.
37 C. Foucher, B. Guilhabert, A. L. Kanibolotsky, P. J. Skabara, N. Laurand and M. D. Dawson, *Opt. Express*, 2016, **24**, 2273.
38 A. Adamow, A. Szukalski, L. Sznitko, L. Persano, D. Pisignano, A. Camposeo and J. Mysliwiec, *Light Sci. Appl.*, 2020, **9**, 2–9.
39 H. Zhang, Q. Su and S. Chen, *Nat. Commun.*, 2020, **11**, 2826.
40 J. Guan, R. Li, X. G. Juarez, A. D. Sample, Y. Wang, G. C. Schatz and T. W. Odom, *Adv. Mater.*, 2021, 2103262.
41 S. Chen, X. Zhao, Y. Wang, J. Shi and D. Liu, *Appl. Phys. Lett.*, 2012, **101**, 123508.
42 X. Shi, Y. Bian, J. Tong, D. Liu, J. Zhou and Z. Wang, *Opt. Express*, 2020, **28**, 13576.
43 X. Qin, J. Xu, Y. Wu and X. Liu, *ACS Cent. Sci.*, 2019, **5**, 29–42.
44 H. Dong, L. D. Sun and C. H. Yan, *Chem. Soc. Rev.*, 2015, **44**, 1608–1634.
45 H. Dong, L. D. Sun and C. H. Yan, *Front. Chem.*, 2021, **8**, 1–8.
46 D. Przybylska, A. Ekner-Grzyb, B. F. Grześkowiak and T. Grzyb, *Sci. Rep.*, 2019, **9**, 8669.
47 K. Wang, J. Jiang, S. Wan and J. Zhai, *Electrochim. Acta*, 2015, **155**, 357–363.
48 M. Osuchowski, F. Osuchowski, W. Latos and A. Kawczyk-Krupka, *Life*, 2021, **11**, 1–11.
49 B. S. Richards, D. Hudry, D. Busko, A. Turshatov and I. A. Howard, *Chem. Rev.*, 2021, **121**, 9165–9195.
50 L. Nucara, F. Greco and V. Mattoli, *J. Mater. Chem. C*, 2015, **3**, 8449.
51 B. Sikora, Zaprojektowanie i Scharakteryzowanie Biosensorów Opartych Na Koloidalnych Nanocząstkach Do Zastosowań w Biologii i Medycynie, Instytut Fizyki Polskiej Akademii Nauk, 2013.
52 S. Cotton, *Lanthanide and Actinide Chemistry*, John Wiley & Sons, Ltd, 2006.
53 R. M. Pallares and R. J. Abergel, *Nanoscale*, 2020, **12**, 1339–1348.
54 J. F. Suyver, A. Aebischer, D. Biner, P. Gerner, J. Grimm, S. Heer, K. W. Krämer, C. Reinhard and H. U. Güdel, *Opt. Mater.*, 2005, **27**, 1111–1130.
55 J. H. Zeng, J. Su, Z. H. Li, R. X. Yan and Y. D. Li, *Adv. Mater.*, 2005, **17**, 2119–2123.
56 P. L. A. M. Corstjens, S. Li, M. Zuiderwijk, K. Kardos, W. R. Abrams, R. S. Niedbala and H. J. Tanke, *IEE Proc.: Nanobiotechnol.*, 2005, **152**, 64–72.
57 H. Zhang, Y. Li, Y. Lin, Y. Huang and X. Duan, *Nanoscale*, 2011, **3**, 963–966.
58 K. W. Krämer, D. Biner, G. Frei, H. U. Güdel, M. P. Hehlen and S. R. Lüthi, *Chem. Mater.*, 2004, **16**, 1244–1251.
59 F. Wang and X. Liu, *J. Am. Chem. Soc.*, 2008, **130**, 5642–5643.
60 Y. Wang, L. Tu, J. Zhao, Y. Sun, X. Kong and H. Zhang, *J. Phys. Chem. C*, 2009, **113**, 7164–7169.
61 C. T. Chen, C. C. Liu, C. H. Wang, C. W. Chen and Y. F. Chen, *Appl. Phys. Lett.*, 2011, **98**, 261918.
62 G. Haider, H. I. Lin, K. Yadav, K. C. Shen, Y. M. Liao, H. W. Hu, P. K. Roy, K. P. Bera, K. H. Lin, H. M. Lee, Y. T. Chen, F. R. Chen and Y. F. Chen, *ACS Nano*, 2018, **12**, 11847.
63 C. Zhang, L. Yang, J. Zhao, B. Liu, M. Y. Han and Z. Zhang, *Angew. Chem., Int. Ed.*, 2015, **54**, 1–8.
64 S. Y. Lim, W. Shen and Z. Gao, *Chem. Soc. Rev.*, 2015, **44**, 362–381.
65 H. Ding, S. B. Yu, J. S. Wei and H. M. Xiong, *ACS Nano*, 2016, **10**, 484–491.
66 K. P. Goetz, A. D. Taylor, F. Paulus and Y. Vaynzof, *Adv. Funct. Mater.*, 2020, **30**, 1910004.
67 L. Protesescu, S. Yakunin, M. I. Bodnarchuk, F. Krieg, R. Caputo, C. H. Hendon, R. X. Yang, A. Walsh and M. V. Kovalenko, *Nano Lett.*, 2015, **15**, 3692–3696.
68 S. M. Morris, P. J. Hands, S. Findeisen-Tandel, R. H. Cole, T. D. Wilkinson and H. J. Coles, *Opt. Express*, 2008, **16**, 18827–18837.

69 X. Zhan, F. F. Xu, Z. Zhou, Y. Yan, J. Yao and Y. S. Zhao, *Adv. Mater.*, 2021, **33**(37), 2104418.
70 S. Süsstrunk, R. Buckley and S. Swen, *Proc. IS&T/SID 7th Color Imaging Conference*, 1999, **7**, 127–134.
71 H. L. Dai, C. Yin, Z. Y. Xiao, Z. Q. Cao and X. F. Chen, *Phys. Rev. Appl.*, 2019, **11**, 064055.
72 J. Mysliwiec, M. Durko-Maciag, A. Popczyk, A. Szukalska, A. Szukalski, Y. Bretonniere, C. Andraud, G. Ulrich and J. Massue, Proceedings Volume 12274, Emerging Imaging and Sensing Technologies for Security and Defence VII; 2022, 1227414.
73 J. J. Wu, M. P. Zhuo, R. Lai, S. N. Zou, C. C. Yan, Y. Yuan, S. Y. Yang, G. Q. Wei, X. D. Wang and L. S. Liao, *Angew. Chem.*, 2021, **60**(16), 9114–9119.
74 P. Zhou and K. Han, *Aggregate*, 2022, **3**(5), e160.
75 P. Gayathri, M. Pannipara, A. G. Al-Sehemi and S. P. Anthony, *CrystEngComm*, 2021, **23**, 3771–3789.
76 Y. Fan, C. Zhang, Z. Gao, W. Zhou, Y. Hou, Z. Zhou, J. Yao and Y. S. Zhao, *Adv. Mater.*, 2021, **21**, 2102586.
77 J. J. Wu, H. Gao, R. Lai, M. P. Zhuo, J. Feng, X. D. Wang, Y. Wu, L. S. Liao and L. Jiang, *Matter*, 2020, **2**, 1233–1243.
78 Q. Dai, C. E. Duty and M. Z. Hu, *Small*, 2010, **6**, 1577–1588.
79 A. Tabuchi, T. Hayakawa, S. Kuwata, R. Ishige and S. Ando, *Mater. Adv.*, 2021, **2**, 5629–5638.
80 M. Mathivanan, B. Tharmalingam, C. H. Lin, B. V. Pandiyan, V. Thiagarajan and B. Murugesapandian, *CrystEngComm*, 2020, **22**, 213–228.
81 E. S. Moraes, L. G. Teixeira Alves Duarte, J. C. Germino and T. D. Z. Atvars, *J. Phys. Chem. C*, 2020, **124**(41), 22406–22415.
82 K. C. Tang, M. J. Chang, T. Y. Lin, H. A. Pan, T. C. Fang, K. Y. Chen, W. Y. Hung, Y. H. Hsu and P. T. Chou, *J. Am. Chem. Soc.*, 2011, **133**(44), 17738–17745.
83 M. P. Zhuo, Y. Su, Y. K. Qu, S. Chen, G. P. He, Y. Yuan, H. Liu, Y. C. Tao, X. D. Wang and L. S. Liao, *Adv. Mater.*, 2021, **33**, 2102719.
84 A. L. Alvarado-Leaños, D. Cortecchia, C. N. Saggau, S. Martani, G. Folpini, E. Feltri, M. D. Albaqami, L. Ma and A. Petrozza, *ACS Nano*, 2022, **16**(12), 20671–20679.
85 M. P. Mamaeva, A. Y. Samsonova, A. O. Murzin, O. A. Lozhkina, A. A. Murashkina, N. I. Selivanov and Y. V. Kapitonov, *J. Phys. Chem. C*, 2022, **126**(46), 19816–19821.
86 J. Liang, Y. Du, K. Wang, A. Ren, X. Dong, C. Zhang, J. Tang, Y. Yan and Y. S. Zhao, *Adv. Opt. Mater.*, 2022, **10**, 2101642.
87 K. Qasim, B. Wang, Y. Zhang, P. Li, Y. Wang, S. Li, S. T. Lee, L. S. Liao, W. Lei and Q. Bao, *Adv. Funct. Mater.*, 2017, **27**, 1606874.
88 S. A. Veldhuis, P. P. Boix, N. Yantara, M. Li, T. C. Sum, N. Mathews and S. G. Mhaisalkar, *Adv. Mater.*, 2016, **28**, 6804–6834.
89 C. Zou, C. Chang, D. Sun, K. F. Böhringer and L. Y. Lin, *Nano Lett.*, 2020, **20**(5), 3710–3717.
90 Q. Pan, J. Fu, S. Liu, J. Zhou, B. Ma, S. Chen, Y. Qiu, Y. Lin, Y. Hu, D. Yang, J. Chen, M. K. Fung, Y. Wang, Q. Zhang, L. Wang and M. Cao, *Cell Reports Phys. Sci.*, 2023, **4**, 101275.
91 K. Wang, Y. Du, J. Liang, J. Zhao, F. F. Xu, X. Liu, C. Zhang, Y. Yan and Y. S. Zhao, *Adv. Mater.*, 2020, **32**, 2001999.
92 A. E. Zhukov, N. V. Kryzhanovskaya, E. I. Moiseev and M. V. Maximov, *Light Sci. Appl.*, 2021, **10**, 2–11.
93 Y. Wang, V. D. Ta, K. S. Leck, B. H. I. Tan, Z. Wang, T. He, C. D. Ohl, H. V. Demir and H. Sun, *Nano Lett.*, 2017, **17**(4), 2640–2646.
94 Z. Wang, M. Cao, G. Shao, Z. Zhang, H. Yu, Y. Chen, Y. Zhang, Y. Li, B. Xu, Y. Wang and J. Yao, *J. Phys. Chem. Lett.*, 2020, **11**, 767–774.
95 H. W. Hu, G. Haider, Y. M. Liao, P. K. Roy, R. Ravindranath, H. T. Chang, C. H. Lu, C. Y. Tseng, T. Y. Lin, W. H. Shih and Y. F. Chen, *Adv. Mater.*, 2017, **29**, 1703549.
96 M. Cao, Y. Zhang, X. Song, Y. Che, H. Zhang, C. Yan, H. Dai, G. Liu, G. Zhang and J. Yao, *Nanotechnology*, 2016, **27**, 1–9.
97 J. L. Zhu, W. H. Li, Y. Sun, J. G. Lu, X. L. Song, C. Y. Chen, Z. Zhang and Y. Su, *Appl. Phys. Lett.*, 2015, **106**, 191903.
98 P. J. W. Hands, D. J. Gardiner, S. M. Morris, C. Mowatt, T. D. Wilkinson and H. J. Coles, *Appl. Phys. Lett.*, 2011, **98**, 141102.
99 D. J. Gardiner, S. M. Morris, P. J. W. Hands, C. Mowatt, R. Rutledge, T. D. Wilkinson and H. J. Coles, *Opt. Express*, 2011, **19**, 2432–2439.
100 Z. Diao, L. Kong, L. Xuan and J. Ma, *Org. Electron.*, 2015, **27**, 101–106.
101 W. Cao, A. Muñoz, P. Palffy-Muhoray and B. Taheri, *Nat. Mater.*, 2002, **1**, 111–113.
102 K.-Y. Yu, S.-H. Chang, C.-R. Lee, T.-Y. Hsu and C.-T. Kuo, *Opt. Mater. Express*, 2014, **4**, 234.
103 S. M. Jeong, K. Sonoyama, Y. Takanishi, K. Ishikawa, H. Takezoe, S. Nishimura, G. Suzaki and M. H. Song, *Appl. Phys. Lett.*, 2006, **89**, 241116.
104 R. Wu, J. Lu, X. Wang, F. Yang, Y. Li and Q. Dai, *Optik*, 2020, **202**, 163616.
105 L. Cerdán, A. Costela, G. Durán-Sampedro, I. García-Moreno, M. Calle, M. Juan-Y-Seva, J. De Abajo and G. A. Turnbull, *J. Mater. Chem.*, 2012, **22**, 8938–8947.
106 L. He, Ş. K. Özdemir and L. Yang, *Laser Photonics Rev.*, 2013, **7**, 60–82.
107 F. Scotognella, A. Monguzzi, M. Cucini, F. Meinardi, D. Comoretto and R. Tubino, *Int. J. Photoenergy*, 2008, **389034**, 1–4.
108 A. Camposeo, M. Polo, P. Del Carro, L. Silvestri, S. Tavazzi and D. Pisignano, *Laser Photonics Rev.*, 2014, **8**, 785–791.
109 J. Feng, W. Wen, X. Wei, X. Jiang, M. Cao, X. Wang, X. Zhang, L. Jiang and Y. Wu, *Adv. Mater.*, 2019, **31**, 1807880.
110 S. Chen, X. D. Wang, M. P. Zhuo, G. Q. Wei, J. J. Wu and L. S. Liao, *Adv. Opt. Mater.*, 2022, **10**, 2101931.
111 C. Fruhling, K. Wang, S. Chowdhury, X. Xu, J. Simon, A. Kildishev, L. Dou, X. Meng, A. Boltasseva and V. M. Shalaev, *Laser Photonics Rev.*, 2023, **17**, 2200314.
112 H. C. Hsu, Z. Y. Wu, Y. Y. Chen and L. J. Lin, *J. Phys. Chem. C*, 2019, **123**(28), 17566–17573.
113 S. Basak, O. Bar-On and J. Scheuer, *Opt. Mater. Express*, 2021, **12**(2), 374–382.
114 W. Gao, Q. Wei, T. Wang, J. Xu, L. Zhuang, M. Li, K. Yao and S. F. Yu, *ACS Nano*, 2022, **16**(8), 13082–13091.

115 X. Tian, L. Wang, W. Li, Q. Lin and Q. Cao, *ACS Appl. Mater. Interfaces*, 2021, **13**(14), 16952–16958.
116 Fan Fan, Sunay Turkdogan, Zhicheng Liu, David Shelhammer and C. Z. Ning, *Nat. Nanotechnol.*, 2015, **10**, 796.
117 F. Fan, Z. Liu, L. Yin, P. L. Nichols, H. Ning, S. Turkdogan and C. Z. Ning, *Semicond. Sci. Technol.*, 2013, **28**, 065005.
118 H. Cao, J. Y. Xu, E. W. Seelig and R. P. H. Chang, *Appl. Phys. Lett.*, 2000, **76**, 2997.
119 D. S. Wiersma and S. Cavalieri, *Nature*, 2001, **414**, 708.
120 D. S. Wiersma, *Nat. Phys.*, 2008, **4**, 359.
121 A. Aigner, J. M. Dawes, S. A. Maier and H. Ren, *Light Sci. Appl.*, 2022, **11**, 145–148.
122 L. Lu, R. E. Simpson and S. K. Valiyaveedu, *J. Opt.*, 2018, **20**, 103001.
123 P. Huo, S. Zhang, Y. Liang, Y. Lu and T. Xu, *Adv. Opt. Mater.*, 2019, **7**, 1801616.
124 S. Lu, L. Sui, Y. Liu, X. Yong, G. Xiao, K. Yuan, Z. Liu, B. Liu, B. Zou and B. Yang, *Adv. Sci.*, 2019, **6**, 1801470.
125 L. Gao, W. Bao, A. V. Kuklin, S. Mei, H. Zhang and H. Ågren, *Adv. Mater.*, 2021, **33**, 2004129.
126 M. Xin, J. Li, Z. Ma, L. Pan and Y. Shi, *Front. Chem.*, 2020, **8**, 1–14.
127 M. M. Tunesi, R. A. Soomro, X. Han, Q. Zhu, Y. Wei and B. Xu, *Nano Converg.*, 2021, **8**, 2–19.
128 A. Iqbal, J. Hong, T. Y. Ko and C. M. Koo, *Nano Converg.*, 2021, **8**, 2–22.
129 S. Tu, M. Mizohata, G. Sheng, L. Liu, F. Ming, C. N. Xu, D. Tu, X. Zhang and H. N. Alshareef, *Adv. Funct. Mater.*, 2020, **30**, 1909843.
130 M. Berggren, D. Nilsson and N. D. Robinson, *Nat. Mater.*, 2007, **6**, 3–5.
131 J. Y. Kim, S. Nagamani, L. Liu, A. H. Elghazaly, N. Solin and O. Inganäs, *Biomacromolecules*, 2020, **21**, 1214–1221.
132 H. W. Chen, J. H. Lee, B. Y. Lin, S. Chen and S. T. Wu, *Light: Sci. Appl.*, 2018, **7**, 17168.
133 M. Riede, D. Spoltore and K. Leo, *Adv. Energy Mater.*, 2021, **11**, 2002653.
134 K. Fukuda, K. Yu and T. Someya, *Adv. Energy Mater.*, 2020, **10**, 2000765.
135 J. Kang, Y. Cho and W. Jang, *Appl. Sci.*, 2021, **11**, 74.
136 A. Salehi, X. Fu, D. H. Shin and F. So, *Adv. Funct. Mater.*, 2019, **29**, 1808803.
137 M. Hecht and F. Würthner, *Acc. Chem. Res.*, 2021, **54**(3), 642–653.
138 C. G. Lu, X. F. Hu, Z. R. Yuan and Y. P. Cui, *RSC Adv.*, 2021, **11**, 12102–12106.
139 D. Punj, R. Regmi, A. Devilez, R. Plauchu, S. B. Moparthi, B. Stout, N. Bonod, H. Rigneault and J. Wenger, *ACS Photonics*, 2015, **2**, 1099–1107.
140 S. Biswas and P. Kumbhakar, *Nanoscale*, 2017, **9**, 18812–18818.
141 H. Song, H. Li and X. Liu, *Opt. Express*, 2018, **26**, 23436–23448.
142 W. Wang, M. Ramezani, A. I. Väkeväinen, P. Törmä, J. G. Rivas and T. W. Odom, *Mater. Today*, 2018, **21**, 303–314.
143 J. Henzie, J. Lee, M. H. Lee, W. Hasan and T. W. Odom, *Annu. Rev. Phys. Chem.*, 2009, **60**, 147–165.
144 M. H. Lee, M. D. Huntington, W. Zhou, J. C. Yang and T. W. Odom, *Nano Lett.*, 2011, **11**(2), 311–315.
145 J. C. Huang, Y. C. Hsiao, Y. T. Lin, C. R. Lee and W. Lee, *Sci. Rep.*, 2016, **6**, 28363.
146 W. F. Zhang, L. Bin Tang, S. F. Yu and S. P. Lau, *Opt. Mater. Express*, 2012, **2**, 490–495.
147 W. Yuan, C. Yin, H. Li, P. Xiao and Z. Cao, *J. Opt. Soc. Am. B*, 2011, **28**(5), 968–971.
148 H. Dai, C. Yin, X. Ye, B. Jiang, M. Ran, Z. Cao and X. Chen, *Sci. Rep.*, 2017, **7**, 3174.
149 International Commission on Illumination. CIE., *Color*. 3rd edn 2004, 552.
150 D. Luo, Q. Chen, B. Liu and Y. Qiu, *Polymers*, 2019, **11**, 384.
151 N. Guan, X. Dai, A. Messanvi, H. Zhang, J. Yan, E. Gautier, C. Bougerol, F. H. Julien, C. Durand, J. Eymery and M. Tchernycheva, *ACS Photonics*, 2016, **3**(4), 597–603.
152 P. Görrn, M. Lehnhardt, W. Kowalsky, T. Riedl and S. Wagner, *Adv. Mater.*, 2011, **23**, 869–872.
153 I. D. W. Samuel and G. A. Turnbull, *Chem. Rev.*, 2007, **107**, 1272.
154 E. L. Hsiang, Z. Yang, Q. Yang, Y. F. Lan and S. T. Wu, *J. Soc. Inf. Disp.*, 2021, **29**, 446–465.
155 F. Zhu, X. T. Hao, O. K. Soo, Y. Li and L. W. Tan, *Proc. IEEE*, 2005, **93**, 1440–1446.
156 A. Hemaida, A. Ghosh, S. Sundaram and T. K. Mallick, *Sol. Energy*, 2020, **195**, 185–193.
157 G. Petriashvili, M. P. De Santo, R. J. Hernandez, R. Barberi and G. Cipparrone, *Soft Matter*, 2017, **13**, 6227–6233.
158 L. Li and L. Deng, *Phys. B*, 2012, **407**, 4826.
159 F. Ahmad, M. Jamil and Y. J. Jeon, *Arab. J. Chem.*, 2017, **10**, S3394–S3401.
160 L. Ryglowski, K. Cyprych and J. Mysliwiec, *Opt. Commun.*, 2022, **510**, 127939.
161 D. Zhang, Z. Chen and D. Ma, *J. Appl. Phys.*, 2008, **103**, 123103.
162 J. Zhao, Y. Yan, Z. Gao, Y. Du, H. Dong, J. Yao and Y. S. Zhao, *Nat. Commun.*, 2019, **10**, 1–7.
163 C. Lee, M. S. Islim, S. Videv, A. Sparks, B. Shah, P. Rudy, M. McLaurin, H. Haas and J. Raring, Advanced LiFi Technology: Laser Light Proceedings, 2020, **11302**, 1130213.
164 H. Haas, E. Sarbazi, H. Marshoud and J. Fakidis, *Opt. Fiber Telecommun. VII*, 2019, 443–493.
165 H. Haas, in 2016 IEEE Photonics Conf. IPC 2016, 2017.
166 H. Haas, L. Yin, Y. Wang and C. Chen, *J. Light Technol.*, 2016, **34**, 1533–1544.
167 H. Haas, *Rev. Phys.*, 2018, **3**, 26–31.
168 H. Cao, Y. G. Zhao, S. T. Ho, E. W. Seelig, Q. H. Wang and R. P. H. Chang, *Phys. Rev. Lett.*, 1999, **82**, 2278.
169 K. Wang and Y. S. Zhao, *Chem*, 2021, **7**, 3221–3231.
170 Q. Zhang, W. Tao, J. Huang, R. Xia and J. Cabanillas-Gonzalez, *Adv. Photonics Res.*, 2021, **2**(5), 2000155.
171 I. Bhattacharjee, N. Acharya, H. Bhatia and D. Ray, *J. Phys. Chem. Lett.*, 2018, **7**(9), 2733–2738.
172 D. Duan, C. Ge, M. Z. Rahaman, C. H. Lin, Y. Shi, H. Lin, H. Hu and T. Wu, *NPG Asia Mater.*, 2023, **15**, 2–22.
173 N. Acharya, M. Upadhyay, S. Dey and D. Ray, *J. Phys. Chem. C*, 2023, **127**(15), 7536–7545.